

# The Madden-Julian Oscillation in the Energy Exascale Earth System Model Version 1

Daehyun Kim<sup>1</sup>, Daehyun Kang<sup>2</sup>, Min-Seop Ahn<sup>3</sup>, Charlotte DeMott<sup>4</sup>, Chia-Wei Hsu<sup>4</sup>, Changhyun Yoo<sup>5</sup>, L. Ruby Leung<sup>6</sup>, Samson Hagos<sup>7</sup>, and Philip Rasch<sup>6</sup>

<sup>1</sup>University of Washington

<sup>2</sup>Chonnam National University

<sup>3</sup>Lawrence Livermore National Laboratory

<sup>4</sup>Colorado State University

<sup>5</sup>Ehwa Womans University

<sup>6</sup>PNNL

<sup>7</sup>Pacific Northwest National Laboratory (DOE)

November 26, 2022

## Abstract

The present study examines the characteristics of the MJO events represented in the Energy Exascale Earth System Model version 1 (E3SMv1), DOE's new Earth system model. The coupled E3SMv1 realistically simulates the eastward propagation of precipitation and Moist Static Energy (MSE) anomalies associated with the MJO. As in observation, horizontal moisture advection and longwave radiative feedback are found to be the dominant processes in E3SMv1 that lead to the eastward movement and maintenance of the MSE anomalies, respectively. Modulation of the diurnal cycle of precipitation in the Maritime Continent region by the MJO is also well represented in the model despite systematic biases in the magnitude and phase of the diurnal cycle. On the midlatitude impact of the MJO, E3SMv1 reasonably captures the pattern of the MJO teleconnection across the North Pacific and North America, with improvement in the performance in a high-resolution version, despite the magnitude being a bit weaker than the observed feature. About interannual variability of the MJO, the El Niño-Southern Oscillation (ENSO) modulation of the zonal extent of MJO's eastward propagation, as well as associated changes in the mean state moisture gradient in the tropical west Pacific, is well reproduced in the model. However, MJO in E3SMv1 exhibits no sensitivity to the Quasi-Biennial Oscillation (QBO), with the MJO propagation characteristics being almost identical between easterly QBO and westerly QBO years. Processes that have been suggested as critical to MJO simulation are also examined by utilizing recently developed process-oriented diagnostics.

1  
2  
3 **The Madden-Julian Oscillation**  
4 **in the Energy Exascale Earth System Model Version 1**  
5

6  
7 **Daehyun Kim<sup>1</sup>, Daehyun Kang<sup>2</sup>, Min-Seop Ahn<sup>3</sup>, Charlotte DeMott<sup>4</sup>, Chia-Wei Hsu<sup>4</sup>,**  
8 **Changhyun Yoo<sup>5</sup>, L. Ruby Leung<sup>6</sup>, Samson Hagos<sup>6</sup>, and Philip J. Rasch<sup>f</sup>**  
9

10 <sup>1</sup> Department of Atmospheric Sciences, University of Washington, Seattle, Washington

11 <sup>2</sup> Department of Oceanography, Chonnam National University, Gwangju, South Korea

12 <sup>3</sup> PCMDI, Lawrence Livermore National Laboratory, Livermore, California

13 <sup>4</sup> Department of Atmospheric Science, Colorado State University, Fort Collins, Colorado

14 <sup>5</sup> Department of Climate and Energy Systems Engineering, Ewha Womans University, Seoul,  
15 South Korea

16 <sup>6</sup> Pacific Northwest National Laboratory, Richland, Washington

17  
18 Corresponding author: Daehyun Kim ([daehyun@uw.edu](mailto:daehyun@uw.edu))  
19

20 **Key Points:**

- 21 • E3SMv1 simulates MJOs that exhibit realistic eastward propagation over the Indo-Pacific  
22 warm pool.
- 23 • Modelled processes of the MJO, revealed through column-integrated MSE anomalies,  
24 matches well with those in observation.
- 25 • Impact of the MJO on diurnal precipitation, MJO teleconnections to midlatitudes and  
26 interannual variability of the MJO are examined.

**Abstract**

The present study examines the characteristics of the MJO events represented in the Energy Exascale Earth System Model version 1 (E3SMv1), DOE's new Earth system model. The coupled E3SMv1 realistically simulates the eastward propagation of precipitation and Moist Static Energy (MSE) anomalies associated with the MJO. As in observation, horizontal moisture advection and longwave radiative feedback are found to be the dominant processes in E3SMv1 that lead to the eastward movement and maintenance of the MSE anomalies, respectively. Modulation of the diurnal cycle of precipitation in the Maritime Continent region by the MJO is also well represented in the model despite systematic biases in the magnitude and phase of the diurnal cycle. On the midlatitude impact of the MJO, E3SMv1 reasonably captures the pattern of the MJO teleconnection across the North Pacific and North America, with improvement in the performance in a high-resolution version, despite the magnitude being a bit weaker than the observed feature. About interannual variability of the MJO, the El Niño-Southern Oscillation (ENSO) modulation of the zonal extent of MJO's eastward propagation, as well as associated changes in the mean state moisture gradient in the tropical west Pacific, is well reproduced in the model. However, MJO in E3SMv1 exhibits no sensitivity to the Quasi-Biennial Oscillation (QBO), with the MJO propagation characteristics being almost identical between easterly QBO and westerly QBO years. Processes that have been suggested as critical to MJO simulation are also examined by utilizing recently developed process-oriented diagnostics.

46

**Plain Language Summary**

The United States Department of Energy developed a new computer model that simulates Earth's climate systems, called Energy Exascale Earth System Model version 1 (E3SMv1). This study examines how well the model reproduces the characteristics of the Madden-Julian Oscillation (MJO), a tropical climate phenomenon that impacts weather and climate around the globe. We find that the strength and eastward movement of the MJO is realistically represented in the model. Variability of water vapor and radiation are the dominant processes for the MJO simulation, which agrees well with the real-world observations. Despite some unrealistic features, E3SMv1 successfully simulates the impact of the MJO on tropical precipitation at shorter than daily time scale and on large-scale atmospheric circulation in the midlatitude. The model also exhibits realistic year-to-year changes in east-west expansion of the MJO by the El Niño-Southern Oscillation, while no noticeable changes can be detected when stratospheric wind reverses its direction over the equator in every 1 or 2 years.

60

## 61 **1 Introduction**

62 Extreme weather and climate events, such as landfalling tropical cyclones, cold surges, and  
63 droughts, present a significant threat to heavily populated areas and have profound socio-  
64 economic impacts on many economic sectors, including energy, agriculture, and water resource  
65 management. As the occurrence frequency of extreme events is expected to increase with  
66 greenhouse gas-induced global warming, it is challenging to develop mitigation strategies for  
67 future extreme events. At the heart of those efforts are short-term predictions and long-term  
68 projections of extreme events, whose accuracy and reliability depend strongly on the fidelity of  
69 the numerical models used to produce them.

70 As the dominant source of Earth system predictability at the intraseasonal time scale, the  
71 Madden-Julian oscillation (MJO) (Madden and Julian 1971, 1972) is a known driver of many  
72 types of extreme events all over the globe (Zhang 2013). Examples of the extreme events  
73 affected by the MJO include extreme rainfall (e.g., Jones and Carvalho 2012), flooding (e.g.,  
74 Bond and Vecchi 2003), cold surges (e.g., Jeong et al. 2005), fire (e.g., Reid et al. 2012),  
75 lightning (e.g., Abatzoglou and Brown 2009), tornado (e.g., Thompson and Roundy 2013), and  
76 tropical cyclones (e.g., Klotzbach 2014), and atmospheric rivers (e.g., Zhou et al. 2021; Hagos et  
77 al. 2021b). Given the MJO's bold fingerprint on the location, frequency, and intensity of these  
78 extreme events, a realistic representation of the MJO is arguably a prerequisite for any numerical  
79 weather and climate models to accurately simulate the societally relevant extreme events.

80 The main goal of the present study is to examine the characteristics of the MJO and its  
81 teleconnections in the Energy Exascale Earth System Model version 1 (E3SMv1) (Golaz et al.  
82 2019; Leung et al. 2020), a fully coupled Earth system model developed as part of the ongoing  
83 E3SM program (e3sm.org) of the U.S. Department of Energy. Despite recent collective efforts to  
84 evaluate the performance of the model (Leung et al. 2020 and references therein), its MJO  
85 simulation fidelity has been only briefly documented in Golaz et al. (2019), who showed that the  
86 eastward propagation of the MJO is realistically represented in the ocean-atmosphere coupled  
87 version of E3SMv1 (their Figure 22), in Caldwell et al. (2019), who briefly compared the MJO  
88 in E3SMv1 at low (~100km) and high (~25km) resolutions, and in Orbe et al. (2020), who  
89 compared the MJO among other modes of variability in six U.S. climate models including  
90 E3SMv1. Our study provides the first in-depth analysis of the MJO variability in E3SMv1  
91 simulations.

92 While significant progress has been made in MJO modeling in the past few decades (readers are  
93 referred to Kim and Maloney 2017, and Jiang et al. 2020 for reviews on the history of MJO  
94 modeling), an accurate representation of the MJO and its teleconnections is still one of the most  
95 challenging tasks for many GCMs (Jiang et al. 2015; Ahn et al. 2017, 2020a; Wang et al.  
96 2020a,b). A particular aspect of MJO variability that most contemporary GCMs struggle with is  
97 the poor representation of the MJO interaction with the islands in the Maritime Continent (MC).  
98 The MJO exhibits peculiar behaviors when it propagates across the MC region, with its  
99 propagation sometimes ceasing (e.g., Kim et al. 2014b; Feng et al. 2015; Zhang and Ling 2017;  
100 DeMott et al. 2018; Kerns and Chen 2020) and its convection detouring around the MC islands  
101 toward the summer hemisphere (e.g., Wang and Rui 1990; Wu and Hsu 2009; Kim et al. 2017).  
102 In many GCMs, MJO propagation is disrupted too frequently, suggesting that the 'barrier'  
103 effects of MC islands on the MJO are exaggerated (e.g., Ling et al. 2017). While the land-sea  
104 contrast (e.g., Sobel et al. 2010), the steep topography (e.g., Wu and Hsu 2009), the persistent  
105 diurnal cycle of precipitation in the MC islands (e.g., Hagos et al. 2016; Zhang and Ling 2017),

106 and the mean state moisture gradient on the eastern side of Sumatra and Borneo (e.g., Jiang et al.  
107 2019) have all been suggested as key aspects of the MC that damp MJO variability there, the  
108 leading mechanisms through which the MC islands affect MJO convection remain elusive.  
109 Reviews on this topic can be found in Jiang et al. (2020) and Kim et al. (2021). To our  
110 knowledge, no study has systematically examined how well GCMs simulate the southward  
111 detouring of the MJO during boreal winter.

112 Another aspect of MJO variability that is poorly represented in GCMs is the year-to-year  
113 variability. While many studies have documented how observed MJO events are affected by the  
114 El Niño southern oscillation (ENSO) (e.g., Woolnough et al. 2000; Tam and Lau 2005; Pohl and  
115 Matthews 2007; Gushchina and Dewitte 2012, Wei and Ren 2019; Zhang and Han 2020; Kang et  
116 al. 2021) and the quasi-biennial oscillation (QBO) (Yoo and Son 2016; Son et al. 2017;  
117 Nishimoto and Yoden 2017; Zhang and Zhang 2018; Hendon and Abhik 2018; Martin et al.  
118 2021b), understanding of the underlying mechanisms of MJO modulation by low-frequency  
119 modes remains incomplete. Despite the statistically robust QBO-MJO relationship present in  
120 observations, no existing GCM seems to be able to reproduce the observed QBO-MJO  
121 relationship (Lee and Klingaman 2018; Kim et al. 2020), even with a QBO signal given through  
122 nudging (Martin et al. 2021a). Richter et al. (2019) showed that E3SMv1 simulates a QBO with  
123 a periodicity and amplitude that are shorter and larger, respectively, than observed; nonetheless,  
124 it is worthwhile to investigate whether and how strongly the QBO modulation of the MJO is  
125 simulated in the model.

126 Careful examination of model simulations can provide useful insights not only into the  
127 mechanism of the phenomenon of interest but also into model biases at the process level. Recent  
128 efforts to develop process-oriented MJO simulation diagnostics have emphasized moisture-  
129 convection coupling (e.g., Kim et al. 2014a), the gross moist stability (e.g., Benedict et al. 2014),  
130 cloud-radiation feedback (e.g., Kim et al. 2015), and the horizontal gradient of mean moisture  
131 (Gonzalez and Jiang 2017; Jiang 2017; DeMott et al. 2019; Ahn et al. 2020a; Kang et al. 2020)  
132 as the processes that are crucial for a model to be able to generate MJO variability internally.  
133 Meanwhile, the moist static energy and moisture budget of the MJO in observations/reanalysis  
134 products have also been documented in detail (e.g., Maloney 2009; Kiranmayi and Maloney  
135 2011; Kim et al. 2014b; Sobel et al. 2014; Ren et al. 2021). By focusing on phenomena that are  
136 directly affected by the parameterization schemes of deep convection, clouds, and radiation, the  
137 process-based diagnostics can offer insights as to whether and how the parameterizations need to  
138 be improved. These diagnostics can also help assess whether the model simulates the MJO for  
139 the correct reason.

140 In this study, we will analyze simulations made with E3SMv1 to investigate MJO propagation,  
141 the MJO MSE budget, MJO teleconnections to the mid-latitudes, the interaction of the MJO with  
142 the MC islands, and the MJO-ENSO and MJO-QBO relationships. Processes that have been  
143 suggested as critical to MJO simulation will be examined by utilizing recently developed  
144 process-oriented diagnostics, which can guide further model development.

145 The manuscript is organized as follows. The model simulations and the reference datasets are  
146 described in Section 2. The diagnostics used in the analysis are explained in Section 3. In Section  
147 4, we present the result of performance- and process-based diagnosis of MJO variability in  
148 E3SMv1 simulations, which is followed by a summary and conclusions in Section 5.

## 149 2 Model and Data

### 150 2.1 Reference data

151 In this study, The National Oceanic and Atmospheric Administration (NOAA) daily interpolated  
152 Outgoing Longwave Radiation (OLR) product (Liebmann and Smith 1996) is used as a proxy for  
153 tropical convection. The rain rate is taken from the Tropical Rainfall Measuring Mission  
154 (TRMM) Multi-satellite Precipitation Analysis (TMPA). The TRMM dataset used in this study is  
155 the post-real-time data of version 7 (3B42), with a temporal resolution of 3 hours and spatial  
156 resolution of  $0.25^\circ \times 0.25^\circ$  (Huffman et al. 2007). For sea surface temperature (SST), the Hadley  
157 Centre Sea Ice and Sea Surface Temperature (Rayner et al. 2003) dataset is used.

158 Various atmospheric state variables and the turbulent and radiative fluxes at the lower and upper  
159 boundaries of the atmosphere are obtained from the fifth generation of the European Centre for  
160 Medium-Range Weather Forecasts (ECMWF) reanalysis (ERA5) product (Hersbach et al. 2020).

161 The AVHRR OLR and ERA5 data are obtained for the period 1979–2018, and the TRMM rain  
162 rate for 1998–2018. All data are interpolated onto a  $2.5^\circ$  longitude  $\times$   $2.5^\circ$  latitude horizontal grid.  
163 In this study, we primarily focus on boreal winter from November to April (NDJFMA) when the  
164 MJO and its teleconnection to the extratropics are most pronounced. As an exception to this, the  
165 interannual variability of the MJO is investigated in DJF (Section 4.6).

### 166 2.2 E3SM version 1

167 E3SMv1 has been developed from the Community Earth System Model version 1 (CESM1) and  
168 by including numerous changes in the atmosphere and by replacing ocean, sea ice, and land ice  
169 models, all based on the Model for Prediction Across Scales (MPAS) that uses spherical  
170 centroidal voronoi tessellations for multi-resolution modeling. The E3SMv1 atmosphere model  
171 (EAM, Rasch et al. 2019; Xie et al. 2018) is based on the Community Atmosphere Model  
172 version 5 (CAM5), but with updates to the cloud microphysics, shallow convection, aerosol, and  
173 turbulence parameterizations. The vertical resolution was more than doubled (30 to 72 levels)  
174 and model top raised to allow an improved treatment of the lower stratosphere relative to CAM5.  
175 With the release of E3SMv1 in April 2018 both the low resolution (LR, Golaz et al. 2019) and  
176 high resolution (HR, Caldwell et al. 2019) model versions, where the atmosphere model is  
177 applied at a grid spacing of  $\sim 100\text{km}$  and  $\sim 25\text{km}$ , respectively, are available. The LR and HR  
178 versions of the model use somewhat different parameter settings to optimize model fidelity in the  
179 two model configurations, so differences are not due solely to resolution. Readers are referred to  
180 Leung et al. (2020) and references therein for the overview of development of E3SM and the  
181 evaluation of its performance.

182 Three sets of coupled simulations made with E3SMv1 are analyzed in this study. The 5-member  
183 ensemble Historical (1850–2014) simulation conducted with LR E3SMv1, which is available  
184 from the CMIP6 archive, is used to investigate the interannual variability of the MJO (Section  
185 4.6). While covering a long period (165 years) and thereby providing enough samples for the  
186 examination of year-to-year variability, not all variables needed for detailed process studies are  
187 available from the Historical simulation. By branching off from one ensemble member of the  
188 Historical ensemble simulation, we performed a 20-yr (1995–2014) simulation with LR E3SMv1  
189 by saving many atmospheric variables and turbulent and radiative fluxes at the surface and the  
190 top of the atmosphere at a 6-hourly interval. In addition, a 20-yr (1957–1976) simulation  
191 (Balaguru et al. 2020) made with HR E3SMv1, as an extension of the 50-yr run reported by

192 Caldwell et al. (2019) with time-invariant 1950s forcing, is used. Note that the output from the  
 193 20-year simulations made with LR and HR E3SMv1 are our primary dataset for most  
 194 diagnostics. For the MJO MSE budget and MJO process-oriented diagnostics, only LR E3SMv1  
 195 is examined.

196 Figure 1 shows the longitude-lag diagrams of equatorial (10°S–10°N), intraseasonal precipitation  
 197 anomalies regressed onto the Indian Ocean (5°S–5°N, 85–95°E) reference timeseries from  
 198 observations (Fig. 1a) and from the three model simulations (Figs. 1b-d). The observed eastward  
 199 propagation of intraseasonal precipitation anomalies associated with the MJO (Fig. 1a) is  
 200 reasonably reproduced in all E3SMv1 simulations used in this study (Figs. 1b-d). A feature that  
 201 is worth noting is that the MJO signal in LR E3SMv1 is greater than observed in the MC region  
 202 (110°-140°E), suggesting the MJO experiences a weaker MC barrier effect in the model than in  
 203 the observations. Comparison with HR E3SMv1 indicates that employing a higher horizontal  
 204 resolution did not improve the MJO simulation, consistent with Caldwell et al. (2019) based on  
 205 comparison of the precipitation power spectra at low and high resolutions. HR E3SMv1 features  
 206 a somewhat faster and weaker MJO propagation in the MC region (Fig. 1c). Lastly, MJO  
 207 propagation characteristics are qualitatively similar between the 20-year (Fig. 1b) and the  
 208 Historical ensemble simulations (Fig. 1d).

### 209 **3 Diagnosis of MJO and its teleconnections**

210 In this section, we provide brief descriptions of the specific diagnostics that are used in this study  
 211 to examine processes associated with the MJO and MJO teleconnections.

#### 212 *3.1 MJO life-cycle composite*

213 To extract the MJO signal from observations and model simulations, we use a method that is  
 214 similar to that of Wheeler and Hendon (2004), which is often referred to as the MJO life-cycle  
 215 composite. For each dataset of interest, we obtain the combined empirical orthogonal functions  
 216 (CEOFs) of 15°S-15°N averaged, intraseasonal (20-100 day bandpass filtered) anomalies of  
 217 OLR and zonal wind at 850 and 200-hPa. For model simulation data, the resulting two leading  
 218 CEOFs are rotated to best match the pattern of the observed counterparts. Once the leading pair  
 219 of CEOFs are obtained, the corresponding PCs are used to define the ‘phase’ and ‘amplitude’ of  
 220 the MJO, following Wheeler and Hendon (2004). The MJO life-cycle composite can be  
 221 constructed for any atmospheric field or flux variable by averaging intraseasonal anomalies of  
 222 the variable for each MJO phase (total of 8 “Real-Time Multivariate MJO” (RMM) phases) with  
 223 an amplitude threshold of 1.

#### 224 *3.2 MJO MSE budget*

225 To examine the moistening process associated with the maintenance and propagation of the  
 226 MJO, we use the intraseasonal, vertically-integrated MSE budget equation:

$$227 \left\langle \frac{\partial m}{\partial t} \right\rangle' = -\langle \vec{V} \cdot \nabla_h m \rangle' - \left\langle \omega \frac{\partial m}{\partial p} \right\rangle' + LH' + SH' + \langle LW \rangle' + \langle SW \rangle' + res_m, \quad (1)$$

228 where  $m$  is MSE ( $= C_p T + gz + L_v q$ ),  $C_p$  is the specific heat of dry air at constant pressure,  $g$  is  
 229 the gravitational constant,  $L_v$  is the latent energy of vaporization,  $T$ ,  $q$ ,  $LH$  and  $SH$  are  
 230 temperature, specific humidity, surface latent and sensible heat fluxes, respectively, and  $LW$  and  
 231  $SW$  are longwave and shortwave radiative heating rates, respectively.  $res_m$  is the budget  
 232 residual, which is obtained by subtracting all RHS terms from MSE tendency. The prime

233 indicates an intraseasonal anomaly, and the angle brackets denote the mass-weighted vertical  
 234 integral from the surface to 100 hPa. The MSE budget analysis has been used to examine the  
 235 propagation and maintenance of the MJO in observations and model simulations (e.g., Maloney  
 236 2009; Kiranmayi and Maloney 2011; Andersen and Kuang 2012; Arnold et al. 2013; Kim et al.  
 237 2014b). The relative contribution of the individual MSE budget terms to the maintenance ( $S_m$ )  
 238 and propagation ( $S_p$ ) of MSE anomalies can be estimated by projecting them upon MSE  
 239 anomalies and their tendencies (e.g., Andersen and Kuang 2012):

$$240 \quad S_m(F) = \frac{\|F' \cdot M'\|}{\|M' \cdot M'\|}, \quad (2a)$$

$$241 \quad S_p(F) = \frac{\|F' \cdot \partial M' / \partial t\|}{\|\partial M' / \partial t \cdot \partial M' / \partial t\|}, \quad (2b)$$

242 where  $F'$  and  $M'$  are column-integrated MSE budget terms and MSE anomaly, respectively, and  
 243  $\|A\|$  is the integral of variable A over the domain 60°-180°E, 20°S-10°N, and MJO phases 1-8 in  
 244 the MJO life-cycle composite.

### 245 *3.3 MJO teleconnections*

246 The lagged life-cycle composite is used to analyze the evolution of mid-latitude circulation  
 247 anomalies associated with the MJO. For example, for MJO phase 3, days with an active (i.e.,  
 248 amplitude > 1) MJO are defined as zero lag days, and the lagged composites are constructed by  
 249 averaging 500-hPa geopotential height anomalies for the successive lag days without an MJO  
 250 amplitude constraint. To obtain patterns and daily time series of the Pacific North American  
 251 (PNA) teleconnection, we perform the Rotated Principal Component Analysis with daily 500-  
 252 hPa geopotential height anomalies in the region between 0°N-90°N (Barnston and Livezey 1987;  
 253 Feldstein 2000). In observations and E3SMv1, the PNA pattern emerges as the third and first  
 254 leading modes, respectively (not shown). The PNA index is obtained by projecting the pattern  
 255 onto the daily anomalies over the North Pacific and North America (0°-90°N, 150°E-30°W).

## 256 **4 Results**

### 257 *4.1 Mean state*

258 From a perspective in which the MJO is defined as fluctuations around the climatological  
 259 seasonal cycle, it is reasonable to assume that the mean state would have profound impacts on  
 260 the characteristics of the MJO. In fact, many processes associated with the propagation and  
 261 maintenance of the MJO have been suggested to be strongly affected by various features of the  
 262 mean state, such as the zonal extent of the mean westerly wind near the equator over the warm  
 263 pool (e.g., Inness et al. 2001), gross moist stability (e.g., Benedict et al. 2014), and horizontal  
 264 gradient of mean moisture (e.g., Gonzalez and Jiang 2017; Jiang 2017; DeMott et al. 2019; Ahn  
 265 et al. 2020a, b; Kang et al. 2020). In this subsection, we focus on the mean state over the Indo-  
 266 Pacific warm pool, which consists of two ocean basins - the Indian Ocean and the western  
 267 Pacific - and the archipelago in between, where the convective signal associated with the MJO is  
 268 most active.

269 Figure 2 shows that the mean precipitation, 850-hPa zonal wind and precipitable water are  
 270 reasonably simulated in LR and HR E3SMv1, though there are some systematic biases in each  
 271 field. In the Indian Ocean and west Pacific, both versions of E3SMv1 exhibit a positive and a  
 272 negative precipitation bias on the western and eastern sides of the basins, respectively. As a

273 result, the zonal gradient of the mean precipitation across the Indian Ocean is weaker than  
274 observed, while the opposite is the case in the western Pacific. In the tropical Pacific, especially  
275 to the east of the dateline, the model exhibits wet biases in the subtropics that are straddling a dry  
276 bias near the equator. It is worthwhile to note that this pattern of precipitation bias is common to  
277 many CMIP6 models (e.g., Fig. 1c in Hagos et al. 2021a), suggesting that the bias is rooted in a  
278 systematic bias in the representation of moist physics (Hagos et al. 2021a). The mean westerly  
279 wind in the equatorial Indian Ocean is underestimated in LR E3SMv1, presumably due to the  
280 weaker-than-observed zonal gradient in the mean precipitation. On the contrary, the mean  
281 westerly wind is overestimated in the Maritime Continent (between 100°–140°E) in LR and HR  
282 E3SMv1, with positive and negative precipitation biases prevail on the eastern and western sides  
283 of the region, respectively.

284 The mean precipitable water (PW) bias pattern overall mimics that of the mean precipitation,  
285 with a dry bias prevailing in the Indo-Pacific warm pool area in both version of E3SMv1. It has  
286 been shown in Golaz et al. (2019) and Caldwell et al. (2019) that the LR and HR E3SMv1  
287 exhibit a weak warm SST bias in many parts of the Indo-Pacific warm pool, suggesting that the  
288 dry bias likely stems from the bias in moist physics. The climatological meridional moisture  
289 gradient is steeper in LR E3SMv1 than in ERA5 in the central and eastern Indian Ocean, with the  
290 magnitude of the dry bias being larger in the off-equatorial area than near the equator. In  
291 contrast, the zonal gradient in the mean PW is underestimated in LR and HR E3SMv1 in the  
292 equatorial Indian Ocean. The role of the mean state moisture gradient, especially that of the  
293 meridional gradient, on the propagation of the MJO in E3SMv1 will be further discussed in  
294 Section 4.3.

#### 295 4.2 MJO propagation characteristics

296 Figure 3 shows the MJO life-cycle composite (Section 3.1) of precipitation (shaded) and column  
297 MSE anomalies (contours) for eight MJO phases. For HR E3SMv1, only precipitation anomalies  
298 are shown because the 3-D variables required to calculate MSE are not available. The  
299 geographical distribution of MJO precipitation anomalies is reasonably represented in both  
300 versions of E3SMv1, although their magnitude is underestimated in HR H3SMv1. In  
301 observations, during phase 1, anomalously enhanced convection associated with positive column  
302 MSE anomalies is located in the western and central Indian Ocean. Dry conditions prevail over  
303 the MC region, except in Borneo and Sumatra islands, where both precipitation and column MSE  
304 show near-zero or slightly positive anomalies. LR and HR E3SMv1 successfully capture this  
305 ‘vanguard’ precipitation signal (Peatman et al. 2014) in the MC islands, although its magnitude  
306 and the zonal extent to the east are slightly overestimated.

307 The development of positive precipitation anomalies in the eastern Indian Ocean during MJO  
308 phases 2 and 3 in E3SMv1 is not as pronounced as in observations, possibly due to the dry bias  
309 in the mean state there (Figure 2). A branch of MJO-related anomalous convection in the  
310 equatorial western Pacific appears in phase 3 and matures in phase 4 in the observations. This  
311 development of enhanced convection in the western equatorial Pacific and subsequently along  
312 the intertropical convergence zone occurs mostly in the northern hemisphere. In LR E3SMv1,  
313 the corresponding precipitation anomalies develop earlier than in observations by about 1 MJO  
314 phase (~ 5–8 days), indicating that the stronger-than-observed vanguard effect is related to the  
315 early onset of convection in the northern branch.

316 Another branch of MJO-associated convection anomalies propagates more slowly and mostly to  
317 the south of the equator, which has been described as the ‘detouring’ signal around the MC  
318 islands (e.g., Wang and Rui 1990; Kim et al. 2017). This branch of anomalous convection  
319 reaches the western Pacific in phase 6 and matures in phase 7, about 3 phases (~ 15–24 days)  
320 later than its northern counterpart. LR and HR E3SMv1 capture remarkably well the propagation  
321 of the southern branch along the oceanic channel between the MC islands and Australia in  
322 phases 4 and 5 and the subsequent development of MJO convection along the south Pacific  
323 convergence zone in phases 6 and 7.

#### 324 4.3 MJO MSE budget

325 Intraseasonal variability of column MSE is mainly governed by that of column water vapor in  
326 the tropics (Wolding et al. 2016). In Figure 3, it is shown that precipitation and column MSE  
327 anomalies are positively correlated with each other in observations and in LR E3SMv1,  
328 suggesting that useful insights into the propagation and maintenance of the MJO precipitation  
329 anomalies can be obtained by examining the column MSE budget. Figure 4 shows the MSE  
330 budget terms (Eq. 1) during MJO phases 2 and 3 in observations (left) and LR E3SMv1 (right),  
331 while the relative contribution of each budget term on the propagation and maintenance of MJO  
332 MSE anomalies are displayed in Figure 5.

333 By design, the MSE tendency term is 90 degrees out of phase with MSE anomalies, showing  
334 positive (i.e., moistening) and negative (i.e., drying) tendency to the east and west of positive  
335 MSE anomalies (1st row in Figure 4). In LR E3SMv1, the horizontal and vertical MSE advection  
336 terms contribute dominantly to the propagation of the MJO MSE anomalies (2nd and 3rd rows in  
337 Figure 4), closely mimicking the corresponding observations. It is worthwhile to note that the  
338 horizontal and vertical MSE advection terms appear to play a dominant role in different areas.  
339 Over the MC area, enhanced horizontal advection of MSE appears to the south of the MC  
340 islands, where the southern branch of MJO convection propagates (Figure 3). On the contrary,  
341 vertical MSE advection moistens the eastern part of the MC and the western equatorial Pacific,  
342 mostly north of 5°S, where the northern branch of MJO convection prevails in later phases.

343 In both observations and LR E3SMv1, column-integrated radiative heating anomalies and  
344 surface turbulent heat fluxes partly compensate for the tendency by the advection terms, thereby  
345 opposing the eastward movement of the MSE anomalies (4th and 5th rows in Figure 4). In  
346 E3SMv1, the magnitude of horizontal advection and surface latent heat flux anomalies to the  
347 south of the MC islands is larger than the observed.

348 Regarding the maintenance of the MJO MSE anomalies, the main balance is found between the  
349 two processes that are strongly tied to convection - vertical advection and longwave heating;  
350 longwave heating moistens columns with positive MSE anomalies (Kim et al. 2015; Wolding  
351 and Maloney 2016), while vertical advection exports MSE out of the columns (i.e., positive gross  
352 moist stability, Neelin and Held 1987). The opposing role of the processes is represented  
353 realistically in LR E3SMv1, although the model underestimates the magnitude of anomalous  
354 vertical MSE advection and longwave heating in the eastern Indian ocean, where MJO  
355 convection is weaker.

356 Figure 5 shows the relative contribution from each MSE budget term to the propagation of MSE  
357 anomalies, which is quantified through the pattern projection method (Eq. 2). Consistent with  
358 what Figure 4 indicates, the accelerating effect of horizontal advection and the dragging effect  
359 from latent heat flux feedback is somewhat overestimated in LR E3SMv1. The stabilizing role of

360 vertical MSE advection is weaker than observed, while MJO MSE anomalies are overly damped  
 361 by latent heat flux anomalies. To understand the model-observation discrepancy in the MJO  
 362 MSE budget, the vertical structure of vertical velocity, specific humidity, and zonal wind  
 363 anomalies are examined (Figure 6). Also shown in Figure 6 are the corresponding MSE and LH  
 364 anomalies. While the negative latent heat flux anomalies are located slightly to the east of  
 365 positive MSE anomalies in both observations and in LR E3SMv1, they are larger in magnitude  
 366 and overlap more strongly with positive MSE anomalies in LR E3SMv1, indicating a stronger  
 367 dragging and damping effect (LHF in Figure 5). This difference can be understood in terms of  
 368 how wind anomalies are distributed around MJO convection center. Compared to observations,  
 369 the westerly anomalies to the west of MJO convection are weaker, and the areas of positive MSE  
 370 anomalies are more strongly dominated by easterly anomalies in the model. The easterly  
 371 anomalies reduce wind speed, and hence the latent heat flux, by acting upon the climatological  
 372 westerlies in the region (Figure 2). Meanwhile, the magnitude of the vertical velocity anomalies  
 373 in the areas with positive MSE anomalies in the model is about 30% weaker than the observed,  
 374 explaining the weaker damping effect from vertical MSE advection. The model specific  
 375 humidity anomalies are muted near 850-hPa level where enhanced convection is located, in sharp  
 376 contrast to ERA5, likely contributing to the weaker-than-observed vertical velocity anomalies.

377 Overall, LR E3SMv1 skillfully captures the observed horizontal distribution of individual MSE  
 378 budget terms as well as the relative contributions to the propagation and maintenance of MJO  
 379 MSE anomalies. The results for the other MJO phases are similar (not shown).

#### 380 4.4 Modulation of MC diurnal cycle by the MJO

381 Many recent observational and modeling studies focused on the role of the diurnal cycle of  
 382 convection in the MC islands on the propagation of the MJO (e.g., Hagos et al. 2016; Zhang and  
 383 Ling 2017). It was hypothesized that strong convection over the MC islands associated with the  
 384 diurnal cycle could inhibit oceanic convection nearby and hence block MJO propagation (Zhang  
 385 and Ling 2017). Because anomalous convection associated with the MJO develops mainly over  
 386 water (Sobel et al. 2008, 2010), suppression of MC oceanic convection during MJO phases 3 and  
 387 4 could terminate an MJO event.

388 Figure 7 displays the amplitude and phase of the precipitation diurnal cycle in observations and  
 389 in LR and HR E3SMv1. LR E3SMv1 shows the biases in the diurnal cycle of precipitation in the  
 390 MC region that are common to many global climate models (Baranowski et al. 2019; Xie et al.  
 391 2019; Tang et al. 2021): it underestimates the amplitude of the diurnal cycle while the peak  
 392 phase of the diurnal cycle occurs too early. The peak amplitude of the diurnal cycle in the model  
 393 is less than 50% of what TRMM observations suggest. The weaker-than-observed diurnal cycle  
 394 amplitude over MC islands might explain why the apparent MC damping effect on the MJO is  
 395 less pronounced in LR E3SMv1 (Figure 1). The time of maximum diurnal precipitation occurs a  
 396 few to several hours earlier in the model than in observations over water and the islands. It is  
 397 worthwhile to mention the difference in phasing of the diurnal cycle between LR E3SMv1 (a  
 398 coupled simulation, Figure 7e) and the control simulation made with LR EAMv1 (an uncoupled  
 399 simulation; Figure 12b in Xie et al. 2019); the peak diurnal rain seems to occur a few hours later  
 400 in LR E3SMv1 over the islands than in LR EAMv1. This might suggest that air-sea coupling or  
 401 the mean state changes due to coupling could affect the diurnal cycle timing phase. It is also  
 402 possible that the parameter tuning conducted before freezing the coupled version (Table 1 in  
 403 Golaz et al. 2019) have affected the simulation of the diurnal cycle. The systematic bias in the

404 diurnal cycle amplitude is partly alleviated in HR E3SMv1, presumably because it better resolves  
405 the complex land-sea contrast and steep topography in the region (Figure 7).

406 Although still too weak, the diurnal cycle amplitude almost doubles in HR E3SMv1 when  
407 compared to the low-resolution version. HR E3SMv1 experiences more pronounced MJO MC  
408 barrier effect (Figure 1), possibly due to the stronger mean MC diurnal cycle. However, the peak  
409 phase of the diurnal cycle in HR E3SMv1 is even earlier than in LR E3SMv1, suggesting that  
410 factors other than grid size may affect the phasing of the diurnal cycle.

411 Despite the biases in the amplitude and phase of the diurnal cycle, LR and HR E3SMv1  
412 reasonably capture the modulation of the diurnal cycle amplitude by the MJO (Figure 8),  
413 especially over relatively big islands (Borneo and New Guinea), with the diurnal cycle being  
414 enhanced when the MJO's main convection center is located in the Indian Ocean (phases 1-3)  
415 and western Maritime Continent (phase 4). As in observations, the enhancement of the diurnal  
416 cycle appears to contribute to the vanguard precipitation anomalies (Figure 3) in phases 1 and 2.  
417 Presumably due to the coarse horizontal resolution, the modulation of the diurnal cycle by the  
418 MJO is most pronounced in the center of the islands in LR E3SMv1, whereas in observations  
419 and, to a lesser degree in HR E3SMv1, it is most pronounced in the coastal areas in Sumatra,  
420 Java, and Borneo and over the entire island in Sulawesi and New Guinea, again showing the  
421 benefit of employing a finer grid spacing on resolving the diurnal cycle of precipitation in the  
422 region.

423 Figure 9 shows the average evolution of oceanic and land precipitation in the western Maritime  
424 Continent area (15°S-10°N, 100°-120°E) as functions of the local time and the MJO phase. The  
425 MJO affects the diurnal cycle of MC land and oceanic convection mostly by changing the  
426 amplitude of the diurnal cycle, whereas its impact on the phase of the diurnal cycle (i.e., the local  
427 time when the diurnal precipitation peaks) is minimal. That is, precipitation composites exhibit  
428 substantial changes in their strength by MJO phases while their peaks remain around the same  
429 local time. Figure 9 also shows that oceanic precipitation peaks during MJO phases 4 and 5  
430 while land precipitation maxima take place about 1–2 phases earlier, with the ratio of oceanic to  
431 land precipitation being the largest at MJO phase 5.

#### 432 4.5 MJO teleconnections

433 Observational evidence (e.g., Weickmann 1983) and theoretical understanding (e.g., Hoskins and  
434 Karoly 1981) of the MJO's influence on the extratropical circulation were established in the  
435 early '80s (reviews on this topic are available in Stan et al. 2017 and Jiang et al. 2020). The  
436 systematic fluctuations of mid-latitude circulation associated with the MJO are understood as the  
437 anomalous rotational flow excited by the MJO 'Rossby wave source' (Sardeshmukh and Hoskins  
438 1988), which then propagate through the medium of the extratropical basic state as a stationary  
439 Rossby wave packet (Hoskins and Karoly 1981; Hoskins and Ambrizzi 1993).

440 Consistent with the theoretical understanding, modeling studies of MJO teleconnections  
441 emphasized both accurate representation of MJO diabatic heating (Yoo et al. 2015; Stan and  
442 Straus 2019) and realistic extratropical basic state (Henderson et al. 2017) as key aspects for  
443 GCMs to correctly capture the circulation changes associated with the MJO. Because the two  
444 factors – MJO variability and the mean state – often show tradeoffs with conventional cumulus  
445 parameterization schemes (Kim et al. 2011; Mapes and Neale 2011), modeling MJO  
446 teleconnection presents a challenging problem for any GCM. MJO teleconnections in the  
447 contemporary GCMs are often too strong, too persistent, and extended too far to the east (Wang

448 et al. 2020a). Also, for the MJO's modulation of the Pacific North America (PNA) pattern (e.g.,  
449 Mori and Watanabe 2008), the latitudinal position, zonal extent, and intensity of the Pacific  
450 subtropical jet show some robust relationship with the skill scores for MJO teleconnection in the  
451 models (Wang et al. 2020b).

452 Figure 10 shows 500-hPa geopotential height (Z500) anomalies (shaded) for four selected MJO  
453 phases in observations (left), the LR (middle) HR (right) simulations, together with the mean  
454 state 300-hPa zonal wind (green contours). The geopotential height anomalies are averaged  
455 between 5-9 days after the days with a strong MJO signal (amplitude > 1). The Pacific  
456 subtropical jet is reasonably represented in both E3SMv1 simulations, although it is shifted  
457 slightly southward in LR E3SMv1, especially in the central Pacific. In observations, a negative  
458 and positive PNA pattern appears after MJO phases 3 and 7, respectively, which is realistically  
459 captured by both LR and HR E3SMv1 simulations. Interestingly, HR E3SMv1 seems to perform  
460 better in terms of the pattern and magnitude of MJO-associated Z500 anomalies, despite that  
461 precipitation anomalies associated with the MJO in HR E3SMv1 are weaker than in LR  
462 E3SMv1. The pattern correlations with the observed Z500 anomalies are overall higher in HR  
463 E3SMv1, except for the phase 1 result. The lead-lag relationship of PNA-like circulation  
464 anomalies with the MJO phases are also more realistically simulated in HR than in LR (Figure  
465 11), suggesting that a finer grid spacing might be beneficial for a model to simulate the MJO  
466 teleconnections. For MJO phases 1 and 5, the observed Z500 anomalies are weaker than those  
467 for the other MJO phases (Tseng et al. 2019). The model-observation agreement is also low  
468 during phases 1 and 5 compared to that for phases 3 and 7, except for the eastern US for phase 5,  
469 in which HR E3SMv1 correctly captures the anomalous high.

#### 470 4.6 Interannual variability of the MJO

471 We investigate in this subsection the modulation of MJO propagation characteristics by ENSO  
472 and QBO by utilizing the 5-member ensemble historical simulation made with LR E3SMv1.  
473 Note that the analysis in this subsection is limited to DJF.

##### 474 4.6.1 ENSO-MJO

475 Many studies have examined how ENSO affects the MJO in the past few decades (e.g., (Slingo  
476 et al. 1999). In observations, MJO propagation tends to be damped more strongly over the MC  
477 region in La Niña years (e.g., Tam and Lau 2005; Gushchina and Dewitte 2012; DeMott et al.  
478 2018; Wei and Ren 2019; Klingaman and DeMott 2020; Kang et al. 2021). Figure 12 shows that,  
479 to the east of around 110°E, the MJO OLR anomalies are much weaker during the La Niña years  
480 than in El Niño years. This contrast between El Niño and La Niña years is realistically captured  
481 in E3SMv1, showing that the MJO propagates farther to the east during the El Niño years.

482 Recent studies have emphasized the role of the mean state moisture gradient on the propagation  
483 of the MJO (e.g., DeMott et al. 2018; Klingaman and DeMott 2020; Kang et al. 2021). While  
484 detailed moisture budget analysis is not possible with the long-term historical simulation due to  
485 the unavailability of the required variables, Figure 13 offers clues on how the SST changes  
486 associated with ENSO can affect MJO variability. During El Niño years compared to La Niña  
487 years, the tropical Pacific Ocean experiences anomalously high SST near the equator and  
488 associated PW anomalies that are straddled by weaker cold SST and dry PW anomalies in the  
489 off-equatorial western and central Pacific. This pattern of PW anomalies steepens meridional  
490 gradient on both sides of the equator in the MC and west Pacific (Figure 13, second row). A  
491 steeper mean state meridional moisture gradient would lead to a larger meridional moisture

492 advection per unit meridional wind anomalies, promoting enhanced moisture recharging to the  
493 east of the MJO (Jiang 2017; DeMott et al. 2019; Ahn et al. 2020a; Ahn et al. 2020b; Kang et al.  
494 2021). Also, the ENSO-associated PW anomalies weaken the climatological negative zonal  
495 moisture gradient in the western Pacific (Figure 13, third row). With the weaker negative zonal  
496 moisture gradient, the drying caused by MJO easterly anomalies to the east of MJO convection  
497 would be weaker during El Niño years compared to La Niña years, meaning that the basic state  
498 environment that is favorable for MJO is extended farther to the east. The E3SMv1 results  
499 support the notion that ENSO affects MJO by modulating the mean state moisture gradient.

#### 500 4.6.2 QBO-MJO

501 Figure 14 compares MJO propagation characteristics between the easterly and westerly phases of  
502 QBO (EQBO and WQBO, respectively, hereafter). The propagation of the MJO during EQBO  
503 years is stronger and covers a wider zonal range than during WQBO years in observations (e.g.,  
504 Yoo and Son 2016; Son et al. 2017). As in many other contemporary climate models, the MJO in  
505 E3SMv1 exhibits no sensitivity to the QBO, with MJO propagation characteristics being almost  
506 identical between EQBO and WQBO years (Figure 14), despite that the zonal mean temperature  
507 response to QBO in the upper troposphere and lower troposphere is realistically represented in  
508 E3SMv1 (Figure 15). We also examined the QBO-MJO relationship in the recent decades to see  
509 if the relationship emerges with the greenhouse gas-induced warming (Klotzbach et al. 2019).  
510 Our results showed that while the model could capture the lower stratospheric cooling in the  
511 recent decades, there was no notable trend in the QBO-MJO relationship (not shown). The lack  
512 of the QBO-MJO relationship in E3SMv1 might be due to the bias in the representation of the  
513 QBO, which is too fast and too strong compared to the observed QBO variability (Richter et al.  
514 2019). Hendon and Abhik (2018) proposed a hypothesis that the zonal mean temperature  
515 anomaly associated with the QBO affects the MJO by modulating the strength of the cold cap  
516 above MJO convection. During EQBO years, the cold cap becomes stronger and provides  
517 enhanced positive feedback to anomalous convection, aiding further development. If the model  
518 convection scheme is not sensitive enough to the changes in the upper tropospheric and lower  
519 stratospheric static stability, it is possible that the parent model is unable to simulate the QBO-  
520 MJO relationship even with realistic representations of both.

#### 521 4.7 Process-oriented MJO diagnostics

522 In this section, we present results from selected process-oriented MJO diagnostics that are  
523 designed to offer insights into the process-level bias of the model that may affect its MJO  
524 simulation fidelity. Many process-oriented MJO diagnostics focus on the moist thermodynamics  
525 in the atmosphere, in particular, the interaction among moisture, convection, cloud, and  
526 radiation. For the tropical oceans, the amount of rain over a large area is strongly tied to how  
527 saturated the column is (Bretherton et al. 2004; Peters and Neelin 2006; Rushley et al. 2018),  
528 which leads to a sharp contrast in rain rate between dry and wet columns. Kim et al. (2014)  
529 proposed the relative humidity composite based on precipitation (RHCP) diagnostic to quantify  
530 the strength of the coupling between moisture and precipitation. The RHCP diagnostic displays  
531 the lower free-tropospheric RH (average of 850- and 700-hPa RH) as a function of precipitation  
532 percentile. Figure 16a shows that the model RH is close to the reference (ERA5) overall,  
533 although slightly underestimated in the low precipitation percentiles. The precipitation-moisture  
534 coupling in the model measured as the RH difference between columns with high (upper 10%)  
535 and low (lower 20%) rain rate – the RHCP metric, which is shown to be positively correlated  
536 with MJO performance metrics (e.g., Kim et al. 2014; Jiang et al. 2015; Ahn et al. 2017) is

537 slightly weaker than in ERA5 (38.7% vs. 43.3%), suggesting that enhancing moisture sensitivity  
538 of convection in the model may lead to a stronger MJO (e.g., Kim et al. 2012).

539 The longwave cloud-radiation feedback has been suggested as the dominant maintenance  
540 mechanism of the MJO in many observational and model studies (e.g., Lin and Mapes 2004;  
541 Andersen and Kuang 2012; Sobel et al. 2014). One way of quantifying the strength of the  
542 longwave cloud-radiation feedback is by assessing the ratio between OLR and precipitation  
543 anomalies in the same unit, as an approximation to the ratio between anomalous column-  
544 integrated longwave and condensational heating. Figure 16b displays the ratio as a function of  
545 precipitation anomaly on a log scale, which is referred to as the Greenhouse Enhancement Factor  
546 (GEF) diagnostic in Kim et al. (2015). It was also shown in Kim et al. (2015) that the ratio for  
547 the weak-to-moderate rain rate anomalies ( $1\text{--}5\text{ mm day}^{-1}$ ) – the GEF metric – exhibited a  
548 statistically significant positive correlation with MJO performance measures. LR E3SMv1  
549 underestimates the GEF for precipitation anomalies lower than  $3\text{ mm day}^{-1}$ , while overestimating  
550 it for higher intensity precipitation anomaly bins (Figure 16b). While the GEF metric from LR  
551 E3SMv1 is close to the reference value (0.26 vs. 0.3), the role of the weaker-than-observed GEF  
552 for the columns with weak precipitation anomalies on MJO variability in the model warrants  
553 further investigation.

554 The normalized gross moist stability (NGMS, Raymond et al. 2009) is a measure of how  
555 efficiently a column can export anomalous energy that goes into it through its boundaries (Neelin  
556 and Held 1987). It has been shown that models with a lower NGMS, hence less stable to energy  
557 input, tend to simulate stronger intraseasonal variability and MJO (e.g., Benedict et al. 2014).  
558 Ahn et al. (2017) estimated the NGMS as the ratio between column-integrated vertical MSE  
559 advection to column-integrated vertical dry static energy (DSE) advection using the time- and  
560 warm pool-averaged vertical profiles of MSE, DSE, and pressure velocity. They showed that the  
561 resulting NGMS metric is negatively correlated with MJO performance measure. Figures 16c  
562 show that warm pool averaged pressure velocity from LR E3SMv1 closely matches that from  
563 ERA5. In the MSE profile (Figure 16d), the overall shape is realistically captured in LR  
564 E3SMv1, despite the MSE value is lower than the observed throughout the troposphere  
565 associated with the dry bias (Figure 2). Nonetheless, the model NGMS obtained from the time-  
566 and warm pool-averaged profiles is close to the value from ERA5 (0.27 vs. 0.28), indicating that  
567 one metric – NGMS in this case – is not enough to characterize the simulated mean state. In the  
568 model development point of view, it will be of interest whether the dry bias can be alleviated  
569 without deteriorating the vertical profile of the mean MSE.

## 570 **5 Summary and Conclusions**

571 The Madden-Julian oscillation (MJO), the dominant source of Earth system predictability at the  
572 intraseasonal time scale, is a known driver of many types of extreme events all over the globe.  
573 However, an accurate representation of the MJO and its teleconnections is still one of the most  
574 challenging tasks for many global climate models (GCMs). In the current study, we documented  
575 the performance of the DOE's new Earth system model - the Energy Exascale Earth System  
576 Model version 1 (E3SMv1) in simulating MJO variability and its teleconnections. Simulations  
577 made with low ( $\sim 100\text{-km}$ , LR) and high ( $\sim 25\text{-km}$ , HR) resolution versions of E3SMv1 were  
578 analyzed with respect to their mean states (Section 4.1), MJO propagation characteristics  
579 (Section 4.2), MJO moist static energy (MSE) budgets (Section 4.3), MJO interactions with  
580 maritime continent (MC) islands (Section 4.4), MJO teleconnections to the mid-latitudes

581 (Section 4.5), and MJO regulation by interannual variability (Section 4.6). In addition, selected  
582 process-oriented MJO diagnostics were applied to the low-resolution E3SMv1 (Section 4.7).

583 We found that LR and HR E3SMv1 adequately simulate the eastward propagation of the MJO  
584 over the Indo-Pacific warm pool (Figure 1), despite that MJO convection anomalies are weaker  
585 in the Indian Ocean (Figure 3), which is presumably due to the bias in the mean state moisture  
586 (Figure 2). Interestingly, the widespread dry bias over the Indo-Pacific warm pool (Figure 2)  
587 does not severely affect the model's fidelity to simulate the eastward propagation of the MJO,  
588 suggesting either that the model mean state biases are not critical to MJO simulation or that the  
589 effect of the mean state bias is compensated by errors in other aspects of the model simulation.

590 It was shown that MJO precipitation anomalies in LR E3SMv1 were tightly coupled to column-  
591 integrated MSE anomalies (Figure 3), suggesting that moisture dynamics play a key role in their  
592 maintenance and propagation. The pattern and magnitude of individual MSE budget terms  
593 associated with the MJO in LR E3SMv1 closely mimic those in observations (Figures 4 and 5).  
594 The MSE budget highlighted that horizontal moisture advection, and longwave radiative  
595 feedback were key processes that led to the eastward movement and maintenance of MSE  
596 anomalies in the model, respectively. Despite our finding that the mean state zonal and  
597 meridional moisture gradient is weaker in the model than in observations (Figure 2), horizontal  
598 advection of MSE drives the MJO's eastward propagation more strongly in the model than in  
599 observations, due to the stronger-than-observed MJO wind anomalies in the model (Figure 5).  
600 On the other hand, the damping and dragging effects from latent heat flux feedback were found  
601 to be overestimated in the model, likely due to the bias in the wind-convection relationship  
602 (Figure 6). One contributing factor might be the underestimation of latent heat fluxes in the LR  
603 E3SMv1 surface flux parameterization in low wind conditions. This known deficiency has been  
604 partly alleviated in other versions of E3SM (e.g., Harrop et al, 2018) by using a "gustiness  
605 parameterization" that makes the surface fluxes sensitive to estimates of parameterized subgrid  
606 processes (convection, and turbulence).

607 The LR and HR E3SMv1 exhibited systematic biases in the magnitude and phase of the diurnal  
608 cycle of precipitation in the Maritime Continent (MC) region that are common to many other  
609 contemporary global climate models; the diurnal variation of precipitation was too weak, and it  
610 peaked a few to several hours earlier than observed (Figure 7). Despite the systematic biases,  
611 however, we found that the modulation of the diurnal cycle of precipitation in the MC region by  
612 the MJO was realistically captured in E3SMv1 (Figures 8 and 9), indicating that the model  
613 handles the interactions between large-scale MJO circulation and small-scale convective systems  
614 over the MC region in a realistic manner. The weak diurnal cycle over the MC islands in LR  
615 E3SMv1 might have contributed to the weaker-than-observed MC barrier effects on MJO  
616 (Figure 1), by facilitating the development of oceanic convection (Hagos et al. 2016; Zhang and  
617 Ling 2017).

618 The LR and HR E3SMv1 also reasonably captured the pattern and magnitude of circulation  
619 anomalies in the Pacific North America region while the magnitude was a bit weaker than the  
620 observed, especially for MJO phases 3 and 7 (Figure 10). On the other hand, the model  
621 representation of MJO teleconnection poorly matched the observed for MJO phases 1 and 5,  
622 when the teleconnection is relatively weak and less coherent in the PNA region. Interestingly, the  
623 HR E3SMv1 appeared to perform better than the low-resolution version in terms of the MJO-  
624 PNA relationship (Figure 11), suggesting that better resolving small-scale eddies in the mid-  
625 latitude might help improve MJO teleconnection.

626 As in observations, the zonal extent of the MJO's eastward propagation was strongly modulated  
627 by El Niño-Southern Oscillation (ENSO) in LR E3SMv1 (Figure 12). During El Niño years  
628 compared to La Niña years, the mean state moisture gradient in the tropical west Pacific changed  
629 to favor more effective moisture recharging by horizontal moisture advection to the east of MJO  
630 convection, facilitating further eastward propagation of MJO (Figure 13). Our results support  
631 recent observational and modeling studies that emphasized the role of the mean state moisture  
632 gradient as the critical feature of the mean state for the MJO's propagation.

633 On the contrary, LR E3SMv1, like many other contemporary global climate models, was found  
634 to be unable to capture the strong coupling between MJO and the stratospheric Quasi-Biennial  
635 Oscillation (QBO); MJO propagation characteristics showed no difference between the easterly  
636 QBO and westerly QBO years (Figure 14). The lack of the QBO-MJO coupling in E3SMv1,  
637 which realistically simulates the temperature changes associated with QBO in the upper  
638 troposphere and lower stratosphere (Figure 15), might suggest that the model convection and  
639 cloud parameterizations are missing an important process that is critical for convection to be  
640 sensitive to circulation changes in the upper troposphere and lower stratosphere. Another  
641 possibility is that the QBO influence on MJO variability is hindered because the model QBO  
642 oscillates too fast (Richter et al. 2019), making it difficult for the QBO-associated circulation  
643 changes to serve as the background conditions for MJO. Richter et al. (2019) showed that the  
644 bias in QBO periodicity and amplitude can be alleviated by tuning two key parameters in the  
645 gravity wave parameterization scheme. It will be of great interest to re-visit the MJO-QBO  
646 relationship in a future version of E3SM, in which the modified gravity wave parameterization  
647 will be implemented.

648 Aspects of the model simulation thought to be critical for MJO simulation were analyzed using  
649 recently developed process-oriented diagnostics. LR E3SMv1 slightly underestimates moisture-  
650 convection coupling (Figure 16a), particularly because the lower free-troposphere is not dry  
651 enough for the weak precipitation regimes (i.e., precipitation percentile < 40). Given that models  
652 tend to simulate a stronger MJO with a tighter moisture-convection coupling, our results suggest  
653 the possibility to improve MJO simulation fidelity in the model by enhancing the convection  
654 sensitivity to moisture. The longwave cloud-radiation feedback was found to be underestimated  
655 for weak precipitation anomalies (Figure 16b). Examining clouds in the weakly perturbed  
656 columns is warranted to improve the longwave cloud-radiation feedback, the main maintenance  
657 process for the MJO in the model (Figure 5). It was found that the vertical profiles of the mean  
658 state vertical velocity and moist static energy over the Indo-Pacific warm pool were realistically  
659 represented in LR E3SMv1 (Figures 16c and 16d), despite the dry bias throughout the  
660 troposphere, yielding the NGMS metric that is close to the observed. The good performance in  
661 the mean state overturning circulation likely contributed to the decent performance of the model  
662 in capturing MJO variability.

663 Collectively, our results have demonstrated that E3SMv1 is an excellent community tool to study  
664 the MJO and its associated extreme events in the current and future climates. As a follow-up  
665 study, we have been analyzing the modulation of tropical cyclones by MJO in the high-  
666 resolution E3SMv1 simulation, the results of which will be reported in a separate study.

667

668 **Acknowledgments**

669 D. Kim was supported by the DOE RGMA program (DE-SC0016223), the NOAA CVP program  
 670 (NA18OAR4310300), the NASA MAP program (80NSSC17K0227), and the Brain Pool  
 671 program funded by the Ministry of Science and ICT through the National Research Foundation  
 672 of Korea (NRF-2021H1D3A2A01039352). D. Kang was supported by Sejong Science  
 673 Fellowship funded by the National Research Foundation of Korea (NRF-  
 674 2021R1C1C2004621). Work of the LLNL-affiliated author (M.-S. Ahn) was performed under  
 675 the auspices of the U.S. Department of Energy by Lawrence Livermore National Laboratory  
 676 under Contract DE-AC52-07NA27344 and their efforts were supported by the Regional and  
 677 Global Model Analysis program area of the United States Department of Energy's Office of  
 678 Science. C. DeMott and C.-W. Hsu were supported by the DOE RGMA program (DE-  
 679 SC0020092). C. Yoo were supported by the National Research Foundation of Korea (NRF-  
 680 2018R1A6A1A08025520 and NRF-2019R1C1C1003161). R. Leung, S. Hagos, and P. Rasch  
 681 were also supported by the Office of Science of U.S. Department of Energy Biological and  
 682 Environmental Research as part of the Regional and Global Model Analysis program area.  
 683 PNNL is operated for the Department of Energy by Battelle Memorial Institute under contract  
 684 DE-AC05-76RL01830.

685

686 **Data Availability Statement**

687 The E3SM project, code, simulation configurations, model output, and tools to work with the  
 688 output are described at the website <https://e3sm.org>. Instructions on how to get started running  
 689 E3SM are available at the website <https://e3sm.org/model/running-e3sm/e3sm-quick-start>. All  
 690 model codes may be accessed on the GitHub repository ([https://github.com/E3SM-  
 691 Project/E3SM](https://github.com/E3SM-Project/E3SM)). Model output data are accessible directly on NERSC or through the DOE Earth  
 692 System Grid Federation ([https://esgf-node.llnl.gov/pro-  
 693 jects/e3sm](https://esgf-node.llnl.gov/projects/e3sm)). The sources for various  
 694 observational data used in this study are as follows: TRMM precipitation  
 695 (<https://gpm.nasa.gov/data/directory>), ERA5 reanalysis  
 696 (<https://www.ecmwf.int/en/forecasts/datasets/reanalysis-datasets/era5>), NOAA daily interpolated  
 697 OLR ([https://psl.noaa.gov/data/gridded/data.interp\\_OLR.html](https://psl.noaa.gov/data/gridded/data.interp_OLR.html)), and HadISST  
 698 (<https://www.metoffice.gov.uk/hadobs/hadisst/>).

698

699 **References**

- 700 Abatzoglou, J. T., and T. J. Brown, 2009: Influence of the Madden-Julian Oscillation on  
 701 Summertime Cloud-to-Ground Lightning Activity over the Continental United States. *Mon.*  
 702 *Weather Rev.*, **137**, 3596–3601, <https://doi.org/10.1175/2009MWR3019.1>.
- 703 Ahn, M.-S., D. Kim, K. R. Sperber, I.-S. Kang, E. Maloney, D. Waliser, and H. Hendon, 2017:  
 704 MJO simulation in CMIP5 climate models: MJO skill metrics and process-oriented diagnosis.  
 705 *Clim. Dyn.*, 1–23, <https://doi.org/10.1007/s00382-017-3558-4>.

- 706 —, and Coauthors, 2020a: MJO Propagation Across the Maritime Continent: Are CMIP6  
707 Models Better Than CMIP5 Models? *Geophys. Res. Lett.*, **47**, e2020GL087250,  
708 <https://doi.org/10.1029/2020GL087250>.
- 709 —, D. Kim, Y.-G. Ham, and S. Park, 2020b: Role of Maritime Continent Land Convection on  
710 the Mean State and MJO Propagation. *J. Clim.*, **33**, 1659–1675, <https://doi.org/10.1175/JCLI-D-19-0342.1>.  
711
- 712 Andersen, J. A., and Z. Kuang, 2012: Moist Static Energy Budget of MJO-like Disturbances in  
713 the Atmosphere of a Zonally Symmetric Aquaplanet. *J. Clim.*, **25**, 2782–2804,  
714 <https://doi.org/10.1175/JCLI-D-11-00168.1>.
- 715 Arnold, N. P., Z. Kuang, and E. Tziperman, 2013: Enhanced MJO-like Variability at High SST.  
716 *J. Clim.*, **26**, 988–1001, <https://doi.org/10.1175/JCLI-D-12-00272.1>.
- 717 Balaguru, K., and Coauthors, 2020: Characterizing Tropical Cyclones in the Energy Exascale  
718 Earth System Model Version 1. *J. Adv. Model. Earth Syst.*, **12**, 1–23,  
719 <https://doi.org/10.1029/2019MS002024>.
- 720 Baranowski, D. B., D. E. Waliser, X. Jiang, J. A. Ridout, and M. K. Flatau, 2019: Contemporary  
721 GCM Fidelity in Representing the Diurnal Cycle of Precipitation Over the Maritime  
722 Continent. *J. Geophys. Res. Atmos.*, **124**, 747–769, <https://doi.org/10.1029/2018JD029474>.
- 723 Barnston, A. G., and R. E. Livezey, 1987: Classification, seasonality and persistence of low-  
724 frequency atmospheric circulation patterns. *Mon. Weather Rev.*, **115**, 1083–1126,  
725 [https://doi.org/10.1175/1520-0493\(1987\)115<1083:CSAPOL>2.0.CO;2](https://doi.org/10.1175/1520-0493(1987)115<1083:CSAPOL>2.0.CO;2).
- 726 Benedict, J. J., E. D. Maloney, A. H. Sobel, and D. M. W. Frierson, 2014: Gross Moist Stability  
727 and MJO Simulation Skill in Three Full-Physics GCMs. *J. Atmos. Sci.*, **71**, 3327–3349,  
728 <https://doi.org/10.1175/JAS-D-13-0240.1>.
- 729 Bond, N. A., and G. A. Vecchi, 2003: The Influence of the Madden–Julian Oscillation on  
730 Precipitation in Oregon and Washington\*. *Weather Forecast.*, **18**, 600–613,  
731 [https://doi.org/10.1175/1520-0434\(2003\)018<0600:TIOTMO>2.0.CO;2](https://doi.org/10.1175/1520-0434(2003)018<0600:TIOTMO>2.0.CO;2).
- 732 Bretherton, C. S., M. E. Peters, and L. E. Back, 2004: Relationships between water vapor path  
733 and precipitation over the tropical oceans. *J. Clim.*, **17**, 1517–1528,  
734 [https://doi.org/10.1175/1520-0442\(2004\)017<1517:RBWVPA>2.0.CO;2](https://doi.org/10.1175/1520-0442(2004)017<1517:RBWVPA>2.0.CO;2).
- 735 Caldwell, P. M., A. Mametjanov, Q. Tang, L. P. Van Roekel, J.-C. Golaz, J.-C., W. Lin, et al.,  
736 2019: The DOE E3SM coupled model version 1: Description and results at high resolution.  
737 *Journal of Advances in Modeling Earth Systems*, **11**. <https://doi.org/10.1029/2019MS001870>.
- 738 —, B. O. Wolding, E. D. Maloney, and D. A. Randall, 2018: Atmospheric Mechanisms for  
739 MJO Decay Over the Maritime Continent. *J. Geophys. Res. Atmos.*, **123**, 5188–5204,  
740 <https://doi.org/10.1029/2017JD026979>.
- 741 —, N. P. Klingaman, W. L. Tseng, M. A. Burt, Y. Gao, and D. A. Randall, 2019: The  
742 Convection Connection: How Ocean Feedbacks Affect Tropical Mean Moisture and MJO  
743 Propagation. *J. Geophys. Res. Atmos.*, **124**, 11910–11931,  
744 <https://doi.org/10.1029/2019JD031015>.

- 745 Feldstein, S. B., 2000: The timescale, power spectra, and climate noise properties of  
746 teleconnection patterns. *J. Clim.*, **13**, 4430–4440, [https://doi.org/10.1175/1520-0442\(2000\)013<4430:TTPSAC>2.0.CO;2](https://doi.org/10.1175/1520-0442(2000)013<4430:TTPSAC>2.0.CO;2).  
747
- 748 Feng, J., T. Li, and W. Zhu, 2015: Propagating and Nonpropagating MJO Events over Maritime  
749 Continent. *J. Clim.*, **28**, 8430–8449, <https://doi.org/10.1175/JCLI-D-15-0085.1>.
- 750 Golaz, J. C., and Coauthors, 2019: The DOE E3SM Coupled Model Version 1: Overview and  
751 Evaluation at Standard Resolution. *J. Adv. Model. Earth Syst.*, **11**, 2089–2129,  
752 <https://doi.org/10.1029/2018MS001603>.
- 753 Gonzalez, A. O., and X. Jiang, 2017: Winter mean lower tropospheric moisture over the  
754 Maritime Continent as a climate model diagnostic metric for the propagation of the Madden-  
755 Julian oscillation. *Geophys. Res. Lett.*, **44**, 2588–2596,  
756 <https://doi.org/10.1002/2016GL072430>.
- 757 Gushchina, D., and B. Dewitte, 2012: Intraseasonal Tropical Atmospheric Variability Associated  
758 with the Two Flavors of El Niño. *Mon. Weather Rev.*, **140**, 3669–3681,  
759 <https://doi.org/10.1175/MWR-D-11-00267.1>.
- 760 Hagos, S. M., C. Zhang, Z. Feng, C. D. Burleyson, C. De Mott, B. Kerns, J. J. Benedict, and M.  
761 N. Martini, 2016: The impact of the diurnal cycle on the propagation of Madden-Julian  
762 Oscillation convection across the Maritime Continent. *J. Adv. Model. Earth Syst.*, **8**, 1552–  
763 1564, <https://doi.org/10.1002/2016MS000725>.
- 764 Hagos, S. M., L. R. Leung, O. A. Garuba, C. Demott, B. Harrop, J. Lu, and M.-S. Ahn, 2021a:  
765 The Relationship between Precipitation and Precipitable Water in CMIP6 Simulations and  
766 Implications for Tropical Climatology and Change. *J. Clim.*, **34**, 1587–1600,  
767 <https://doi.org/10.1175/JCLI-D-20-0211.1>.
- 768 Hagos, S., L. R. Leung, O. Garuba, and C. M. Patricola, 2021b: Influence of background  
769 divergent moisture flux on the frequency of North Pacific atmospheric rivers. *J. Clim.*, **34**,  
770 6129–6139, doi:10.1175/jcli-d-21-0058.1.
- 771 Harrop, B. E., P. L. Ma, P. J. Rasch, R. B. Neale, and C. Hannay, 2018: The Role of Convective  
772 Gustiness in Reducing Seasonal Precipitation Biases in the Tropical West Pacific. *J. Adv.  
773 Model. Earth Syst.*, **10**, 961–970, <https://doi.org/10.1002/2017MS001157>.
- 774 Henderson, S. A., E. D. Maloney, and S.-W. Son, 2017: Madden–Julian Oscillation Pacific  
775 Teleconnections: The Impact of the Basic State and MJO Representation in General  
776 Circulation Models. *J. Clim.*, **30**, 4567–4587, <https://doi.org/10.1175/JCLI-D-16-0789.1>.
- 777 Hendon, H. H., and S. Abhik, 2018: Differences in Vertical Structure of the Madden-Julian  
778 Oscillation Associated With the Quasi-Biennial Oscillation. *Geophys. Res. Lett.*, **45**, 4419–  
779 4428, <https://doi.org/10.1029/2018GL077207>.
- 780 Hersbach, H., and Coauthors, 2020: The ERA5 global reanalysis. *Q. J. R. Meteorol. Soc.*, **146**,  
781 1999–2049, <https://doi.org/10.1002/qj.3803>.
- 782 Hoskins, B. J., and D. J. Karoly, 1981: The Steady Linear Response of a Spherical Atmosphere  
783 to Thermal and Orographic Forcing. *J. Atmos. Sci.*, **38**, 1179–1196,  
784 [https://doi.org/10.1175/1520-0469\(1981\)038<1179:TSLROA>2.0.CO;2](https://doi.org/10.1175/1520-0469(1981)038<1179:TSLROA>2.0.CO;2).

- 785 ———, and T. Ambrizzi, 1993: Rossby Wave Propagation on a Realistic Longitudinally Varying  
 786 Flow. *J. Atmos. Sci.*, **50**, 1661–1671, [https://doi.org/10.1175/1520-](https://doi.org/10.1175/1520-0469(1993)050<1661:RWPOAR>2.0.CO;2)  
 787 [0469\(1993\)050<1661:RWPOAR>2.0.CO;2](https://doi.org/10.1175/1520-0469(1993)050<1661:RWPOAR>2.0.CO;2).
- 788 Huffman, G. J., and Coauthors, 2007: The TRMM Multisatellite Precipitation Analysis (TMPA):  
 789 Quasi-global, multiyear, combined-sensor precipitation estimates at fine scales. *J.*  
 790 *Hydrometeorol.*, **8**, 38–55, <https://doi.org/10.1175/JHM560.1>.
- 791 Inness, P. M., J. M. Slingo, S. J. Woolnough, R. B. Neale, and V. D. Pope, 2001: Organization of  
 792 tropical convection in a GCM with varying vertical resolution; implications for the simulation  
 793 of the Madden-Julian Oscillation. *Clim. Dyn.*, **17**, 777–793,  
 794 <https://doi.org/10.1007/s003820000148>.
- 795 Jeong, J.-H., C.-H. Ho, B.-M. Kim, and W.-T. Kwon, 2005: Influence of the Madden-Julian  
 796 Oscillation on wintertime surface air temperature and cold surges in east Asia. *J. Geophys.*  
 797 *Res. Atmos.*, **110**, <https://doi.org/https://doi.org/10.1029/2004JD005408>.
- 798 Jiang, X., 2017: Key processes for the eastward propagation of the Madden-Julian Oscillation  
 799 based on multimodel simulations. *J. Geophys. Res. Atmos.*, **122**, 755–770,  
 800 <https://doi.org/10.1002/2016JD025955>.
- 801 ———, and Coauthors, 2015: Vertical structure and physical processes of the Madden-Julian  
 802 oscillation: Exploring key model physics in climate simulations. *J. Geophys. Res. Atmos.*,  
 803 **120**, 4718–4748, <https://doi.org/10.1002/2014JD022375>.
- 804 ———, H. Su, and D. E. Waliser, 2019: A Damping Effect of the Maritime Continent for the  
 805 Madden-Julian Oscillation. *J. Geophys. Res. Atmos.*, **124**, 13693–13713,  
 806 <https://doi.org/10.1029/2019JD031503>.
- 807 ———, and Coauthors, 2020: Fifty Years of Research on the Madden-Julian Oscillation: Recent  
 808 Progress, Challenges, and Perspectives. *J. Geophys. Res. Atmos.*, **125**, e2019JD030911,  
 809 <https://doi.org/https://doi.org/10.1029/2019JD030911>.
- 810 Jones, C., and L. M. V. Carvalho, 2012: Spatial-intensity variations in extreme precipitation in  
 811 the contiguous United States and the Madden-Julian oscillation. *J. Clim.*, **25**, 4898–4913,  
 812 <https://doi.org/10.1175/JCLI-D-11-00278.1>.
- 813 Kang, D., D. Kim, M.-S. Ahn, R. Neale, J. Lee, and P. J. Gleckler, 2020: The Role of the Mean  
 814 State on MJO Simulation in CESM2 Ensemble Simulation. *Geophys. Res. Lett.*, **47**,  
 815 e2020GL089824, <https://doi.org/10.1029/2020GL089824>.
- 816 ———, ———, ———, and S.-I. An, 2021: The Role of Background Meridional Moisture Gradient on  
 817 the Propagation of the MJO over the Maritime Continent. *J. Clim.*, 1–54,  
 818 <https://doi.org/10.1175/JCLI-D-20-0085.1>.
- 819 Kerns, B. W., and S. S. Chen, 2020: A 20-Year Climatology of Madden-Julian Oscillation  
 820 Convection: Large-Scale Precipitation Tracking From TRMM-GPM Rainfall. *J. Geophys.*  
 821 *Res. Atmos.*, **125**, 1–21, <https://doi.org/10.1029/2019JD032142>.
- 822 Kim, D., A. H. Sobel, E. D. Maloney, D. M. W. Frierson, and I.-S. Kang, 2011: A Systematic  
 823 Relationship between Intraseasonal Variability and Mean State Bias in AGCM Simulations. *J.*  
 824 *Clim.*, **24**, 5506–5520, <https://doi.org/10.1175/2011jcli4177.1>.

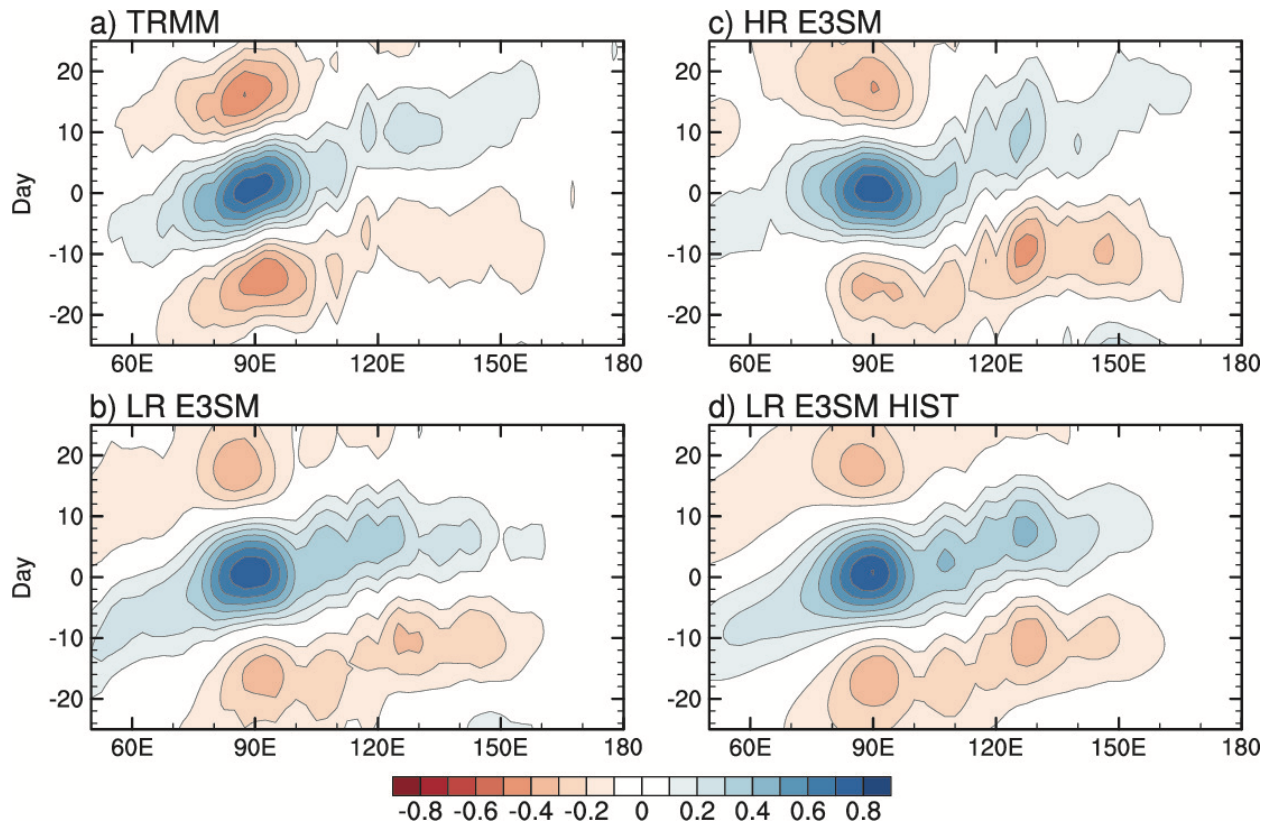
- 825 Kim, D., A. H. Sobel, A. D. Del Genio, Y. Chen, S. J. Camargo, M.-S. Yao, M. Kelley, and L.  
826 Nazarenko, 2012: The Tropical Subseasonal Variability Simulated in the NASA GISS  
827 General Circulation Model. *J. Clim.*, **25**, 4641–4659, [https://doi.org/10.1175/JCLI-D-11-](https://doi.org/10.1175/JCLI-D-11-00447.1)  
828 00447.1.
- 829 ———, and Coauthors, 2014a: Process-Oriented MJO Simulation Diagnostic: Moisture Sensitivity  
830 of Simulated Convection. *J. Clim.*, **27**, 5379–5395, [https://doi.org/10.1175/JCLI-D-13-](https://doi.org/10.1175/JCLI-D-13-00497.1)  
831 00497.1.
- 832 ———, J.-S. Kug, and A. H. Sobel, 2014b: Propagating versus Nonpropagating Madden–Julian  
833 Oscillation Events. *J. Clim.*, **27**, 111–125, <https://doi.org/10.1175/JCLI-D-13-00084.1>.
- 834 ———, M.-S. Ahn, I.-S. Kang, and A. D. Del Genio, 2015: Role of Longwave Cloud–Radiation  
835 Feedback in the Simulation of the Madden–Julian Oscillation. *J. Clim.*, **28**, 6979–6994,  
836 <https://doi.org/10.1175/JCLI-D-14-00767.1>.
- 837 ———, H. Kim, and M.-I. Lee, 2017: Why does the MJO detour the Maritime Continent during  
838 austral summer? *Geophys. Res. Lett.*, **44**, 2579–2587, <https://doi.org/10.1002/2017GL072643>.
- 839 Kim, D. and E. D. Maloney, 2017: Review: Simulation of the Madden-Julian oscillation using  
840 general circulation models, *The Global Monsoon System*, 3rd Edition, C.-P. Chang et al.,  
841 Eds., 119–130.
- 842 Kim, D., E. D. Maloney, and C. Zhang, 2021: Review: MJO propagation over the Maritime  
843 Continent, Chap. 21 in *The Multiscale Global Monsoon System*, Eds: C.P. Chang, K.J. Ha, R.  
844 H. Johnson, D. Kim, G.N. Lau, B. Wang. World Scientific Series on Asia-Pacific Weather  
845 and Climate, Vol. 11. World Scientific, Singapore, <https://doi.org/10.1142/11723>
- 846 Kim, H., J. M. Caron, J. H. Richter, and I. R. Simpson, 2020: The Lack of QBO-MJO  
847 Connection in CMIP6 Models. *Geophys. Res. Lett.*, **47**, 1–8,  
848 <https://doi.org/10.1029/2020GL087295>.
- 849 Kiranmayi, L., and E. D. Maloney, 2011: Intraseasonal moist static energy budget in reanalysis  
850 data. *J. Geophys. Res. Atmos.*, **116**, D21117, <https://doi.org/10.1029/2011JD016031>.
- 851 Klingaman, N. P., and C. A. Demott, 2020: Mean State Biases and Interannual Variability Affect  
852 Perceived Sensitivities of the Madden–Julian Oscillation to Air–Sea Coupling. *J. Adv. Model.*  
853 *Earth Syst.*, **12**, 1–22, <https://doi.org/10.1029/2019MS001799>.
- 854 Klotzbach, P. J., 2014: The Madden–Julian Oscillation’s Impacts on Worldwide Tropical  
855 Cyclone Activity. *J. Clim.*, **27**, 2317–2330, <https://doi.org/10.1175/JCLI-D-13-00483.1>.
- 856 Klotzbach, P., S. Abhik, H. H. Hendon, M. Bell, C. Lucas, A. G. Marshall, and E. C. J. Oliver,  
857 2019: On the emerging relationship between the stratospheric Quasi-Biennial oscillation and  
858 the Madden–Julian oscillation. *Sci. Rep.*, **9**, 1–9, <https://doi.org/10.1038/s41598-019-40034-6>
- 859 Lee, J. C. K., and N. P. Klingaman, 2018: The effect of the quasi-biennial oscillation on the  
860 Madden–Julian oscillation in the Met Office Unified Model Global Ocean Mixed Layer  
861 configuration. *Atmos. Sci. Lett.*, **19**, 1–10, <https://doi.org/10.1002/asl.816>.
- 862 Leung, L. R., D. C. Bader, M. A. Taylor, and R. B. McCoy, 2020: An Introduction to the E3SM  
863 Special Collection: Goals, Science Drivers, Development, and Analysis. *J. Adv. Model. Earth*  
864 *Syst.*, **12**, <https://doi.org/10.1029/2019MS001821>.

- 865 Liebmann, C. A., and B. Smith, 1996: Description of a Complete (Interpolated) Outgoing  
866 Longwave Radiation Dataset. *Bull. Am. Meteorol. Soc.*, **77**, 1275–1277.
- 867 Lin, J. L., and B. E. Mapes, 2004: Radiation budget of the tropical intraseasonal oscillation. *J.*  
868 *Atmos. Sci.*, **61**, 2050–2062, [https://doi.org/10.1175/1520-](https://doi.org/10.1175/1520-0469(2004)061<2050:RBOTTI>2.0.CO;2)  
869 [0469\(2004\)061<2050:RBOTTI>2.0.CO;2](https://doi.org/10.1175/1520-0469(2004)061<2050:RBOTTI>2.0.CO;2)
- 870 Ling, J., C. Zhang, S. Wang, and C. Li, 2017: A new interpretation of the ability of global  
871 models to simulate the MJO. *Geophys. Res. Lett.*, **44**, 5798–5806,  
872 <https://doi.org/10.1002/2017GL073891>.
- 873 Madden, R. A., and P. R. Julian, 1971: Detection of a 40–50 Day Oscillation in the Zonal Wind  
874 in the Tropical Pacific. *J. Atmos. Sci.*, **28**, 702–708, [https://doi.org/10.1175/1520-](https://doi.org/10.1175/1520-0469(1971)028<0702:DOADOI>2.0.CO;2)  
875 [0469\(1971\)028<0702:DOADOI>2.0.CO;2](https://doi.org/10.1175/1520-0469(1971)028<0702:DOADOI>2.0.CO;2).
- 876 ———, and ———, 1972: Description of Global-Scale Circulation Cells in the Tropics with a 40–50  
877 Day Period. *J. Atmos. Sci.*, **29**, 1109–1123, [https://doi.org/10.1175/1520-](https://doi.org/10.1175/1520-0469(1972)029<1109:DOGSCC>2.0.CO;2)  
878 [0469\(1972\)029<1109:DOGSCC>2.0.CO;2](https://doi.org/10.1175/1520-0469(1972)029<1109:DOGSCC>2.0.CO;2).
- 879 Maloney, E. D., 2009: The Moist Static Energy Budget of a Composite Tropical Intraseasonal  
880 Oscillation in a Climate Model. *J. Clim.*, **22**, 711–729,  
881 <https://doi.org/10.1175/2008JCLI2542.1>.
- 882 Mapes, B., and R. Neale, 2011: Parameterizing Convective Organization to Escape the  
883 Entrainment Dilemma. *J. Adv. Model. Earth Syst.*, **3**, <https://doi.org/10.1029/2011ms000042>.
- 884 Martin, Z., C. Orbe, S. Wang, and A. Sobel, 2021a: The MJO-QBO Relationship in a GCM with  
885 Stratospheric Nudging. *J. Clim.*, 1–69, <https://doi.org/10.1175/JCLI-D-20-0636.1>.
- 886 ———, S.-W. Son, A. Butler, H. Hendon, H. Kim, A. Sobel, S. Yoden, and C. Zhang, 2021b: The  
887 influence of the quasi-biennial oscillation on the Madden–Julian oscillation. *Nat. Rev. Earth*  
888 *Environ.*, **2**, 477–489 <https://doi.org/10.1038/s43017-021-00173-9>.
- 889 Mori, M., and M. Watanabe, 2008: The Growth and Triggering Mechanisms of the PNA: A  
890 MJO-PNA Coherence. *J. Meteorol. Soc. Japan. Ser. II*, **86**, 213–236,  
891 <https://doi.org/10.2151/jmsj.86.213>.
- 892 Neelin, J. D., and I. M. Held, 1987: Modeling tropical convergence based on the moist static  
893 energy budget. *Mon. Weather Rev.*, **115**, 3–12, [https://doi.org/10.1175/1520-](https://doi.org/10.1175/1520-0493(1987)115<0003:MTCBOT>2.0.CO;2)  
894 [0493\(1987\)115<0003:MTCBOT>2.0.CO;2](https://doi.org/10.1175/1520-0493(1987)115<0003:MTCBOT>2.0.CO;2).
- 895 Nishimoto, E., and S. Yoden, 2017: Influence of the Stratospheric Quasi-Biennial Oscillation on  
896 the Madden–Julian Oscillation during Austral Summer. *J. Atmos. Sci.*, **74**, 1105–1125,  
897 <https://doi.org/10.1175/JAS-D-16-0205.1>.
- 898 Orbe, C., and Coauthors, 2020: Representation of modes of variability in six U.S. climate  
899 models. *J. Clim.*, **33**, 7591–7617, doi:10.1175/jcli-d-19-0956.1.
- 900 Peatman, S. C., A. J. Matthews, and D. P. Stevens, 2014: Propagation of the Madden–Julian  
901 Oscillation through the Maritime Continent and scale interaction with the diurnal cycle of  
902 precipitation. *Q. J. R. Meteorol. Soc.*, **140**, 814–825, <https://doi.org/10.1002/qj.2161>.
- 903 Peters, O., and J. Neelin, 2006: Critical phenomena in atmospheric precipitation. *Nat. Phys.*, **2**,  
904 393–396, <https://doi.org/10.1038/nphys314>.

- 905 Pohl, B., and A. J. Matthews, 2007: Observed Changes in the Lifetime and Amplitude of the  
 906 Madden–Julian Oscillation Associated with Interannual ENSO Sea Surface Temperature  
 907 Anomalies. *J. Clim.*, **20**, 2659–2674, <https://doi.org/10.1175/JCLI4230.1>.
- 908 Rasch, P. J., and Coauthors, 2019: An Overview of the Atmospheric Component of the Energy  
 909 Exascale Earth System Model. *J. Adv. Model. Earth Syst.* **11**, 2377–2411.  
 910 <https://doi.org/10.1029/2019MS001629>.
- 911 Raymond, D. J., S. L. Sessions, A. H. Sobel, and Ž. Fuchs, 2009: The mechanics of gross moist  
 912 stability. *J. Adv. Model. Earth Syst.*, **1**, <https://doi.org/10.3894/JAMES.2009.1.9>.
- 913 Rayner, N. A., D. E. Parker, E. B. Horton, C. K. Folland, L. V. Alexander, D. P. Rowell, E. C.  
 914 Kent, and A. Kaplan, 2003: Global analyses of sea surface temperature, sea ice, and night  
 915 marine air temperature since the late nineteenth century. *J. Geophys. Res. Atmos.*, **108**, 4407,  
 916 <https://doi.org/10.1029/2002JD002670>.
- 917 Reid, J. S., and Coauthors, 2012: Multi-scale meteorological conceptual analysis of observed  
 918 active fire hotspot activity and smoke optical depth in the Maritime Continent. *Atmos. Chem.*  
 919 *Phys.*, **12**, 2117–2147, <https://doi.org/10.5194/acp-12-2117-2012>.
- 920 Ren, P., D. Kim, M.-S. Ahn, D. Kang, and H.-L. Ren, 2021: Intercomparison of MJO Column  
 921 Moist Static Energy and Water Vapor Budget among Six Modern Reanalysis Products. *J.*  
 922 *Clim.*, **34**, 2977–3001, <https://doi.org/10.1175/JCLI-D-20-0653.1>.
- 923 Richter, J. H., C. C. Chen, Q. Tang, S. Xie, and P. J. Rasch, 2019: Improved Simulation of the  
 924 QBO in E3SMv1. *J. Adv. Model. Earth Syst.*, **11**, 3403–3418,  
 925 <https://doi.org/10.1029/2019MS001763>.
- 926 Rushley, S. S., D. Kim, C. S. Bretherton, and M.-S. Ahn, 2018: Reexamining the nonlinear  
 927 moisture-precipitation relationship over the tropical oceans. *Geophys. Res. Lett.*, **45**, 1133–  
 928 1140, <https://doi.org/10.1002/2017GL076296>.
- 929 Sardeshmukh, P. D., and B. J. Hoskins, 1988: The Generation of Global Rotational Flow by  
 930 Steady Idealized Tropical Divergence. *J. Atmos. Sci.*, **45**, 1228–1251,  
 931 [https://doi.org/10.1175/1520-0469\(1988\)045<1228:TGOGRF>2.0.CO;2](https://doi.org/10.1175/1520-0469(1988)045<1228:TGOGRF>2.0.CO;2).
- 932 Slingo, J. M., D. P. Rowell, K. R. Sperber, and F. Nortley, 1999: On the predictability of the  
 933 interannual behaviour of the Madden-Julian oscillation and its relationship with el Niño. *Q. J.*  
 934 *R. Meteorol. Soc.*, **125**, 583–609, <https://doi.org/10.1002/qj.49712555411>.
- 935 Sobel, A., S. Wang, and D. Kim, 2014: Moist Static Energy Budget of the MJO during  
 936 DYNAMO. *J. Atmos. Sci.*, **71**, 4276–4291, <https://doi.org/10.1175/JAS-D-14-0052.1>.
- 937 Sobel, A. H., E. D. Maloney, G. Bellon, and D. M. Frierson, 2008: The role of surface heat  
 938 fluxes in tropical intraseasonal oscillations. *Nat. Geosci.*, **1**, 653–657.
- 939 ———, ———, ———, and ———, 2010: Surface fluxes and tropical intraseasonal variability: A  
 940 reassessment. *J. Adv. Model. Earth Syst.*, **2**, 2, <https://doi.org/10.3894/JAMES.2010.2.2>.
- 941 Son, S.-W., Y. Lim, C. Yoo, H. H. Hendon, and J. Kim, 2017: Stratospheric Control of the  
 942 Madden–Julian Oscillation. *J. Clim.*, **30**, 1909–1922, <https://doi.org/10.1175/JCLI-D-16-0620.1>.
- 943

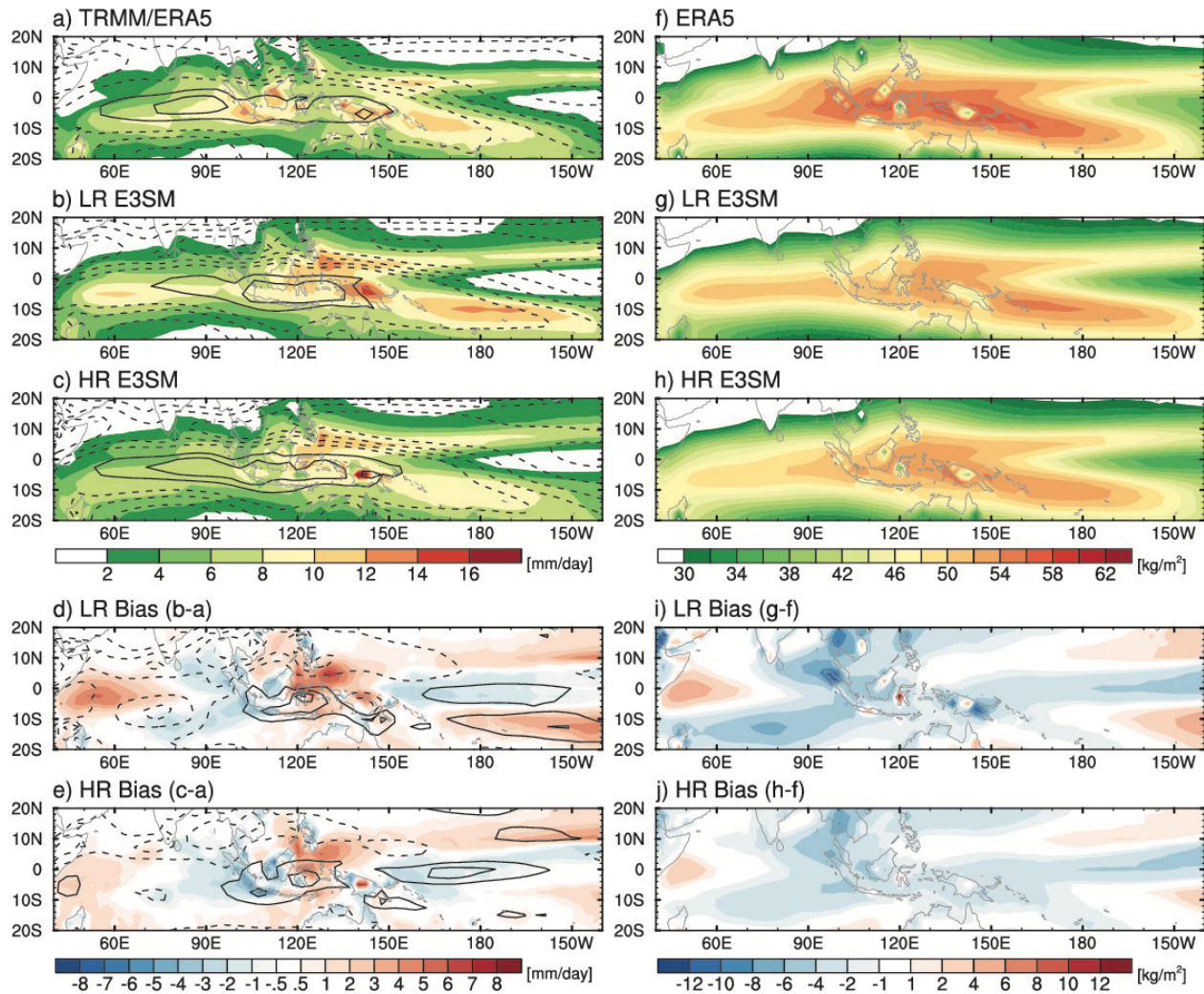
- 944 Stan, C., and D. M. Straus, 2019: The Impact of Cloud Representation on the Sub-Seasonal  
945 Forecasts of Atmospheric Teleconnections and Preferred Circulation Regimes in the Northern  
946 Hemisphere. *Atmosphere-Ocean*, **57**, 233–248,  
947 <https://doi.org/10.1080/07055900.2019.1590178>.
- 948 ———, D. M. Straus, J. S. Frederiksen, H. Lin, E. D. Maloney, and C. Schumacher, 2017: Review  
949 of Tropical-Extratropical Teleconnections on Intraseasonal Time Scales. *Rev. Geophys.*, **55**,  
950 902–937, <https://doi.org/10.1002/2016RG000538>.
- 951 Tam, C.-Y., and N.-C. Lau, 2005: Modulation of the Madden-Julian Oscillation by ENSO:  
952 Inferences from Observations and GCM Simulations. *J. Meteorol. Soc. Japan. Ser. II*, **83**,  
953 727–743, <https://doi.org/10.2151/jmsj.83.727>.
- 954 Tang, S., P. Gleckler, S. Xie, J. Lee, M.-S. Ahn, C. Covey, and C. Zhang, 2021: Evaluating  
955 Diurnal and Semi-Diurnal Cycle of Precipitation in CMIP6 Models Using Satellite- and  
956 Ground-Based Observations. *J. Clim.*, 1–56, <https://doi.org/10.1175/JCLI-D-20-0639.1>.
- 957 Thompson, D. B., and P. E. Roundy, 2013: The Relationship between the Madden-Julian  
958 Oscillation and U.S. Violent Tornado Outbreaks in the Spring. *Mon. Weather Rev.*, **141**,  
959 2087–2095, <https://doi.org/10.1175/MWR-D-12-00173.1>.
- 960 Tseng, K.-C., E. Maloney, and E. Barnes, 2019: The Consistency of MJO Teleconnection  
961 Patterns: An Explanation Using Linear Rossby Wave Theory. *J. Clim.*, **32**, 531–548,  
962 <https://doi.org/10.1175/JCLI-D-18-0211.1>.
- 963 Wang, B., and H. Rui, 1990: Synoptic climatology of transient tropical intraseasonal convection  
964 anomalies: 1975–1985. *Meteorol. Atmos. Phys.*, **44**, 43–61,  
965 <https://doi.org/10.1007/BF01026810>.
- 966 Wang, J., H. Kim, D. Kim, S. A. Henderson, C. Stan, and E. D. Maloney, 2020a: MJO  
967 Teleconnections over the PNA Region in Climate Models. Part I: Performance- and Process-  
968 Based Skill Metrics. *J. Clim.*, **33**, 1051–1067, <https://doi.org/10.1175/JCLI-D-19-0253.1>.
- 969 ———, ———, ———, ———, ———, and ———, 2020b: MJO Teleconnections over the PNA Region in  
970 Climate Models. Part II: Impacts of the MJO and Basic State. *J. Clim.*, **33**, 5081–5101,  
971 <https://doi.org/10.1175/JCLI-D-19-0865.1>.
- 972 Wei, Y., and H. L. Ren, 2019: Modulation of ENSO on fast and slow MJO modes during boreal  
973 winter. *J. Clim.*, **32**, 7483–7506, <https://doi.org/10.1175/JCLI-D-19-0013.1>.
- 974 Weickmann, K. M., 1983: Intraseasonal Circulation and Outgoing Longwave Radiation Modes  
975 During Northern Hemisphere Winter. *Mon. Weather Rev.*, **111**, 1838–1858,  
976 [https://doi.org/10.1175/1520-0493\(1983\)111<1838:ICAOLR>2.0.CO;2](https://doi.org/10.1175/1520-0493(1983)111<1838:ICAOLR>2.0.CO;2).
- 977 Wheeler, M. C., and H. H. Hendon, 2004: An All-Season Real-Time Multivariate MJO Index:  
978 Development of an Index for Monitoring and Prediction. *Mon. Weather Rev.*, **132**, 1917–  
979 1932, [https://doi.org/10.1175/1520-0493\(2004\)132<1917:AARMMI>2.0.CO;2](https://doi.org/10.1175/1520-0493(2004)132<1917:AARMMI>2.0.CO;2).
- 980 Wolding, B. O., E. D. Maloney, and M. Branson, 2016: Vertically resolved weak temperature  
981 gradient analysis of the Madden-Julian Oscillation in SP-CESM. *J. Adv. Model. Earth Syst.*,  
982 **8**, 1586–1619, <https://doi.org/10.1002/2016MS000724>.

- 983 Woolnough, S. J., J. M. Slingo, and B. J. Hoskins, 2000: The Relationship between Convection  
984 and Sea Surface Temperature on Intraseasonal Timescales. *J. Clim.*, **13**, 2086–2104,  
985 [https://doi.org/10.1175/1520-0442\(2000\)013<2086:TRBCAS>2.0.CO;2](https://doi.org/10.1175/1520-0442(2000)013<2086:TRBCAS>2.0.CO;2).
- 986 Wu, C.-H., and H.-H. Hsu, 2009: Topographic Influence on the MJO in the Maritime Continent.  
987 *J. Clim.*, **22**, 5433–5448, <https://doi.org/10.1175/2009JCLI2825.1>.
- 988 Xie, S., and Coauthors, 2018: Understanding Cloud and Convective Characteristics in Version 1  
989 of the E3SM Atmosphere Model. *J. Adv. Model. Earth Syst.*, **10**, 2618–44.  
990 <https://doi.org/10.1029/2018MS001350>.
- 991 —, and Coauthors, 2019: Improved diurnal cycle of precipitation in E3SM with a revised  
992 convective triggering function. *J. Adv. Model. Earth Syst.*, **11**, 2290–2310.  
993 <https://doi.org/10.1029/2019MS001702>.
- 994 Yoo, C., and S.-W. Son, 2016: Modulation of the boreal wintertime Madden-Julian oscillation by  
995 the stratospheric quasi-biennial oscillation. *Geophys. Res. Lett.*, **43**, 1392–1398,  
996 <https://doi.org/10.1002/2016GL067762>.
- 997 —, S. Park, D. Kim, J.-H. Yoon, and H.-M. Kim, 2015: Boreal Winter MJO Teleconnection in  
998 the Community Atmosphere Model Version 5 with the Unified Convection Parameterization.  
999 *J. Clim.*, **28**, 8135–8150, <https://doi.org/10.1175/JCLI-D-15-0022.1>.
- 1000 Zhang, C., 2013: Madden–Julian Oscillation: Bridging Weather and Climate. *Bull. Am.*  
1001 *Meteorol. Soc.*, **94**, 1849–1870, <https://doi.org/10.1175/BAMS-D-12-00026.1>.
- 1002 —, and J. Ling, 2017: Barrier Effect of the Indo-Pacific Maritime Continent on the MJO:  
1003 Perspectives from Tracking MJO Precipitation. *J. Clim.*, **30**, 3439–3459,  
1004 <https://doi.org/10.1175/JCLI-D-16-0614.1>.
- 1005 —, and B. Zhang, 2018: QBO-MJO Connection. *J. Geophys. Res. Atmos.*, **123**, 2957–2967,  
1006 <https://doi.org/10.1002/2017JD028171>.
- 1007 Zhang, L., and W. Han, 2020: Barrier for the Eastward Propagation of Madden-Julian Oscillation  
1008 Over the Maritime Continent: A Possible New Mechanism. *Geophys. Res. Lett.*, **47**, 1–12,  
1009 <https://doi.org/10.1029/2020GL090211>.
- 1010 Zhou, Y., H. Kim, and D. E. Waliser, 2021: Atmospheric river lifecycle responses to the  
1011 Madden-Julian Oscillation. *Geophys. Res. Lett.*, **48**, e2020GL090983.  
1012 <https://doi.org/10.1029/2020GL090983>
- 1013
- 1014



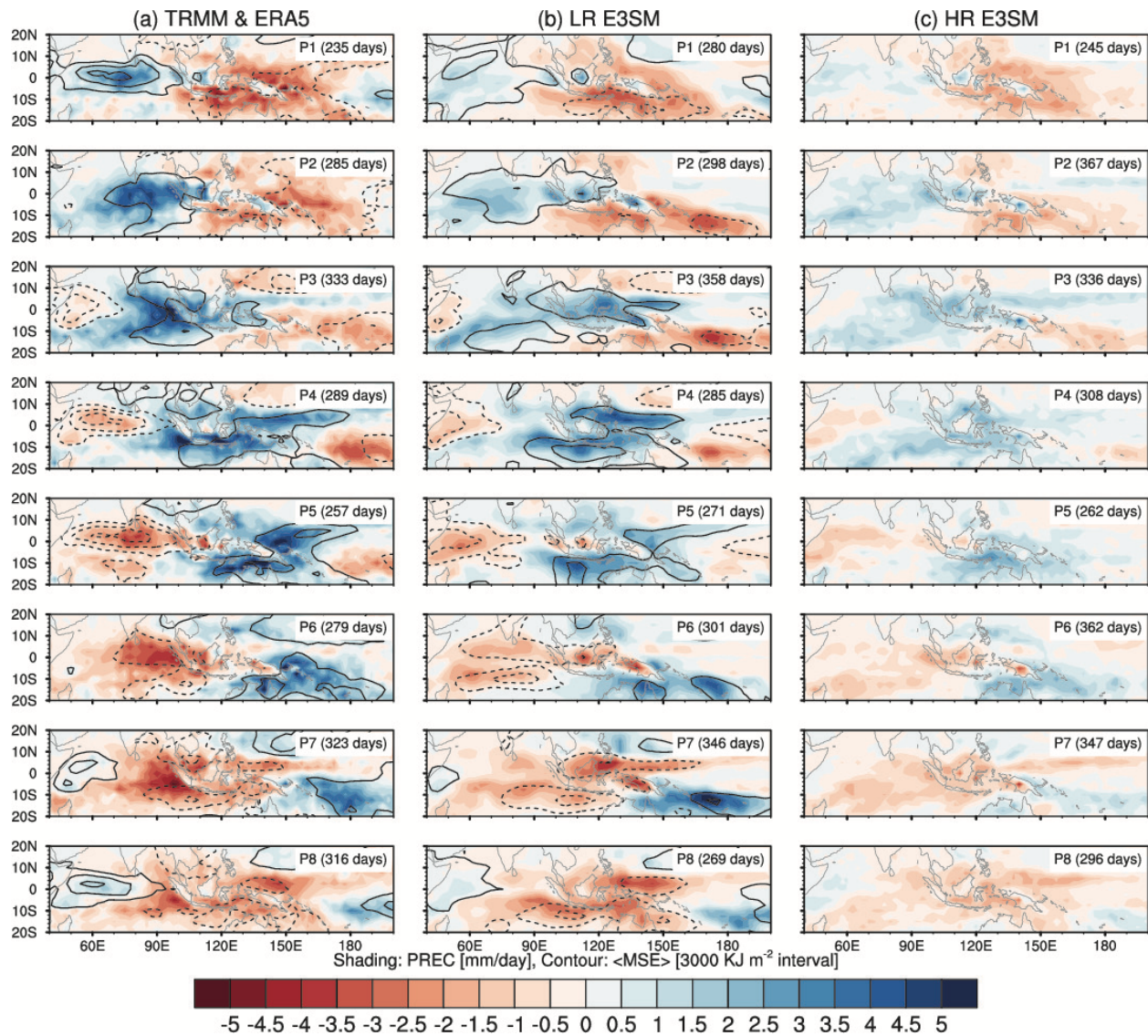
1015

1016 **Figure 1.** Longitude–lag diagram of equatorial ( $10^{\circ}\text{S}$ – $10^{\circ}\text{N}$ ) precipitation regressed against  
 1017 intraseasonal precipitation anomalies in the Indian Ocean reference region ( $5^{\circ}\text{S}$ – $5^{\circ}\text{N}$ ,  $85$ – $95^{\circ}\text{E}$ )  
 1018 during NDJFMA for (a) TRMM and (b)–(d) E3SMv1 model simulations. For (b) and (c) LR and  
 1019 HR simulations of a recent 20-year period are used, while for (d) the 5-ensemble CMIP6  
 1020 Historical simulation (1850–2014) made with LR E3SMv1 is used.



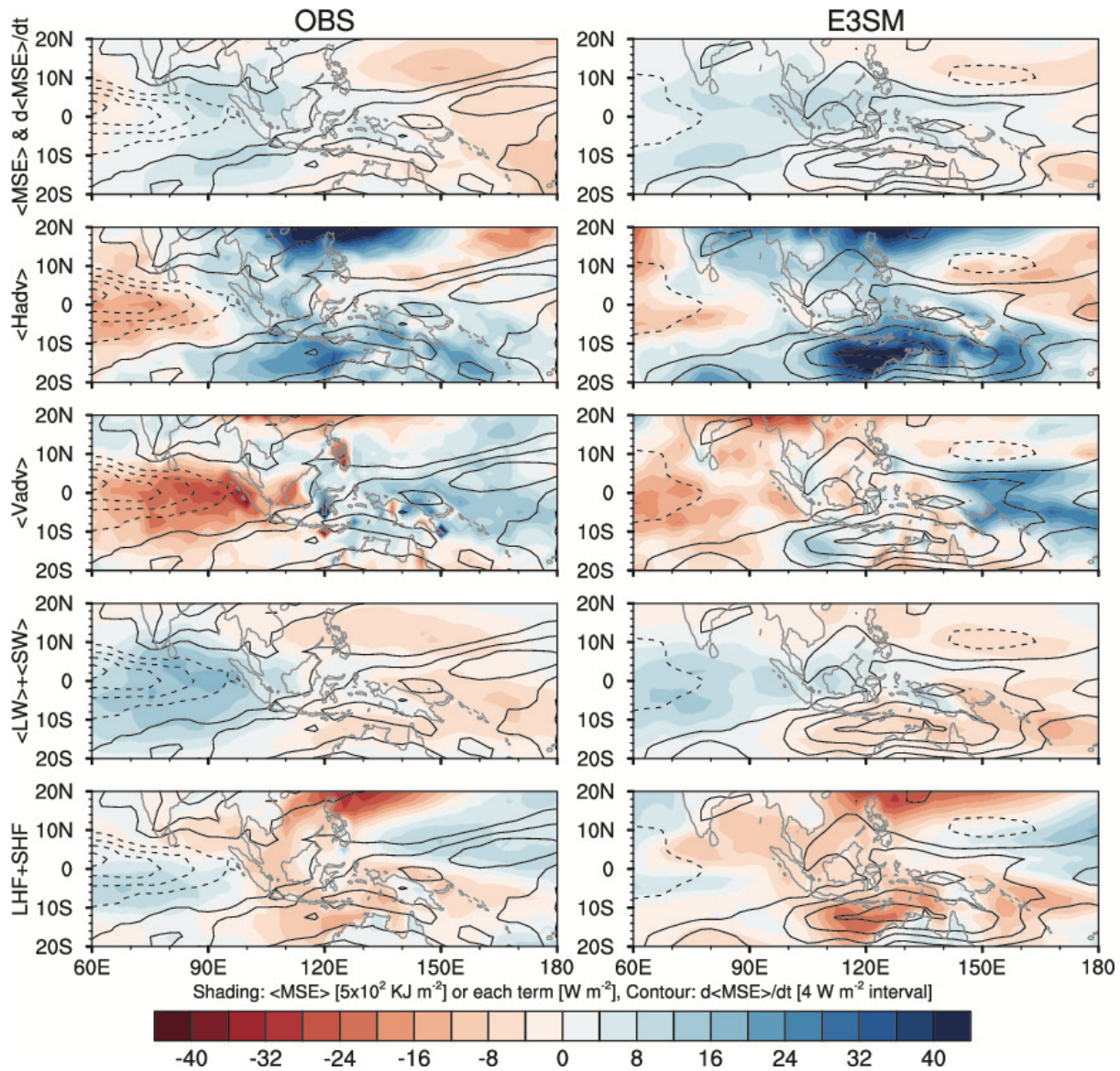
1021

1022 **Figure 2.** November-April mean state of (a, b, and c) precipitation ( $\text{mm day}^{-1}$ , shaded) and 850-  
 1023 hPa zonal wind ( $\text{m s}^{-1}$ , contour), and (f, g, and h) precipitable water ( $\text{kg m}^{-2}$ , shaded). The top  
 1024 three panels show observations, LR E3SMv1, and HR E3SMv1, respectively, while the bottom  
 1025 two row show the biases in LR E3SMv1 and HR E3SMv1, respectively. The contour interval for  
 1026 850-hPa zonal wind is  $2 \text{ m s}^{-1}$ . For the bias, the contour intervals are  $1 \text{ m s}^{-1}$  for 850-hPa zonal  
 1027 wind and the zero lines are omitted.



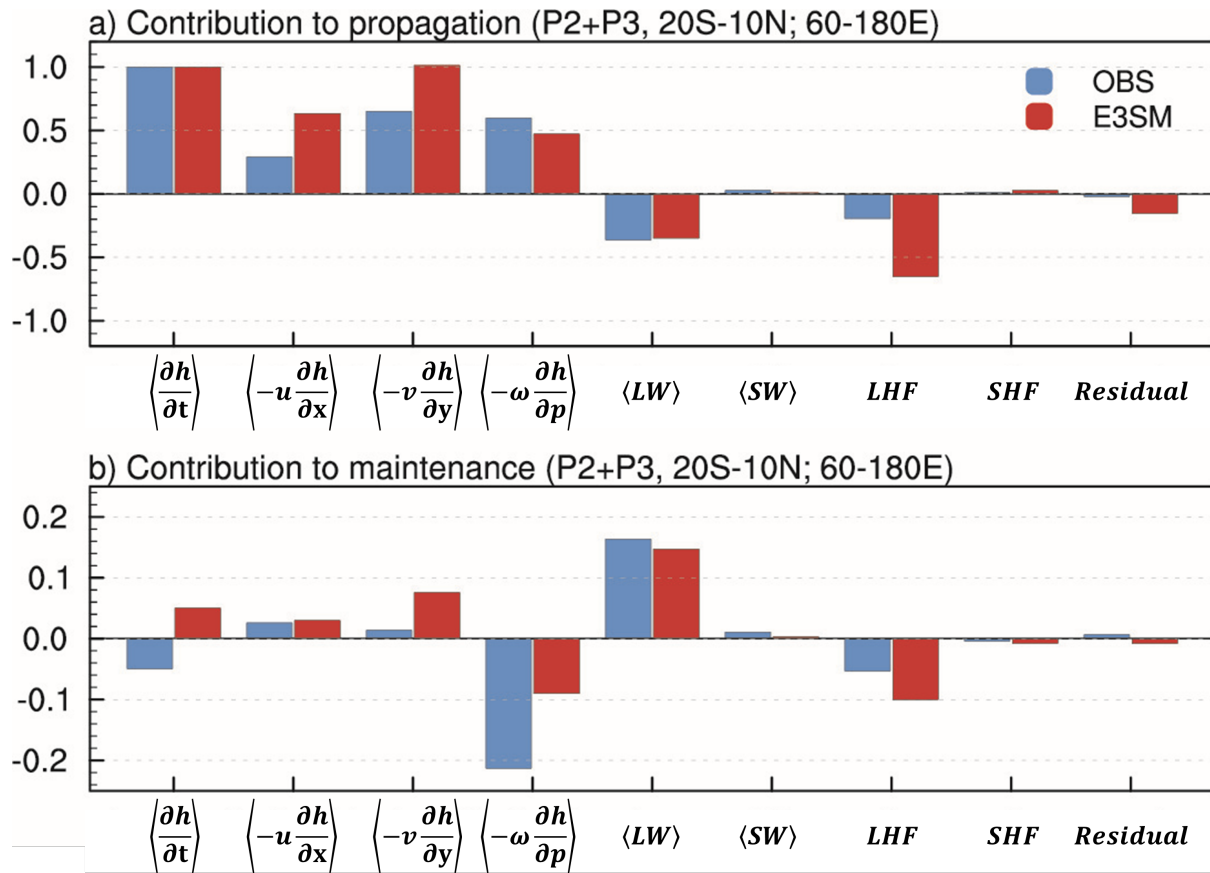
1028

1029 **Figure 3.** MJO life cycle composite maps of intraseasonal precipitation ( $\text{mm day}^{-1}$ , shaded) and  
 1030 column-integrated MSE anomalies ( $\text{kJ m}^{-2}$ , contour) obtained from each RMM phase (RMM  
 1031 amplitude  $> 1$ ) during NDJFMA: a) observations, b) LR E3SMv1, and c) HR E3SMv1. The  
 1032 contour interval for column-integrated MSE anomalies is  $3000 \text{ KJ m}^{-2}$ . The number of days used  
 1033 in each phase composite is indicated in the parentheses.



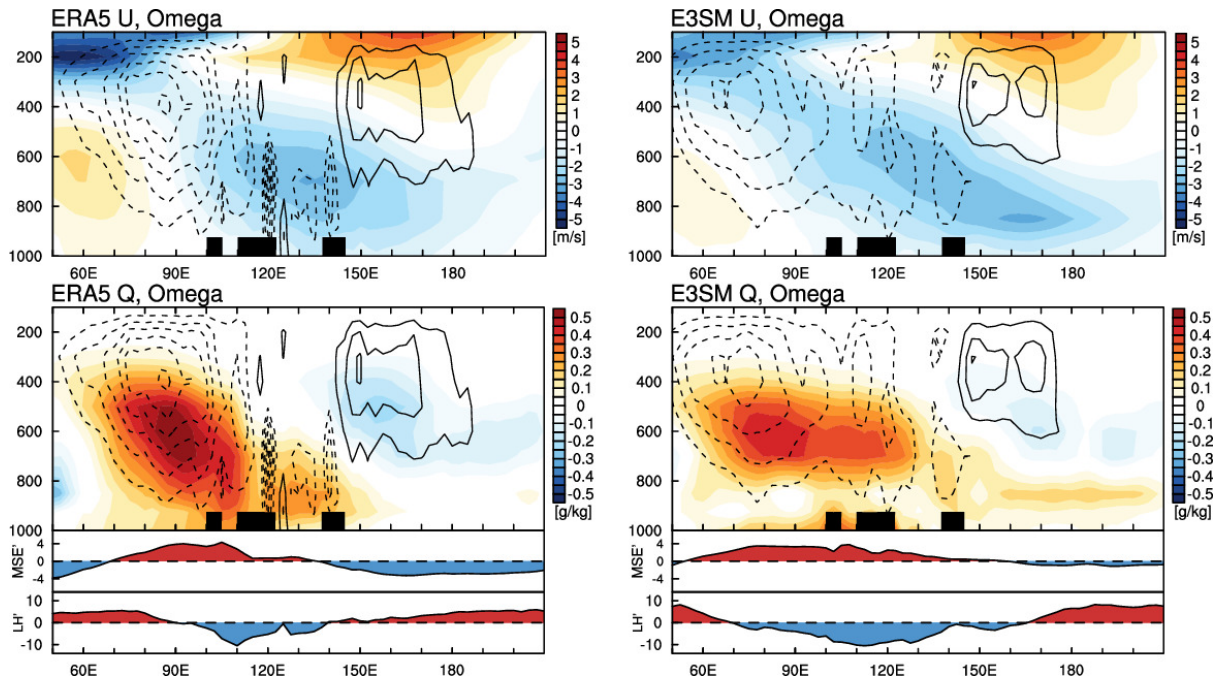
1034

1035 **Figure 4.** (1<sup>st</sup> row) Column-integrated MSE anomalies ( $\text{kJ m}^{-2}$ , shaded) and total MSE tendency  
 1036 ( $\text{kJ m}^{-2}$ , contour) composited for MJO phases 2 and 3: (left) ERA5 and (right) LR E3SMv1. (2<sup>nd</sup>  
 1037 to 5<sup>th</sup> rows) Same as the 1<sup>st</sup> row, except that shading indicates horizontal advection, vertical  
 1038 advection, radiative heating, and surface turbulent fluxes, respectively. The contour interval for  
 1039 total MSE tendency is  $4 \text{ W m}^{-2}$ .



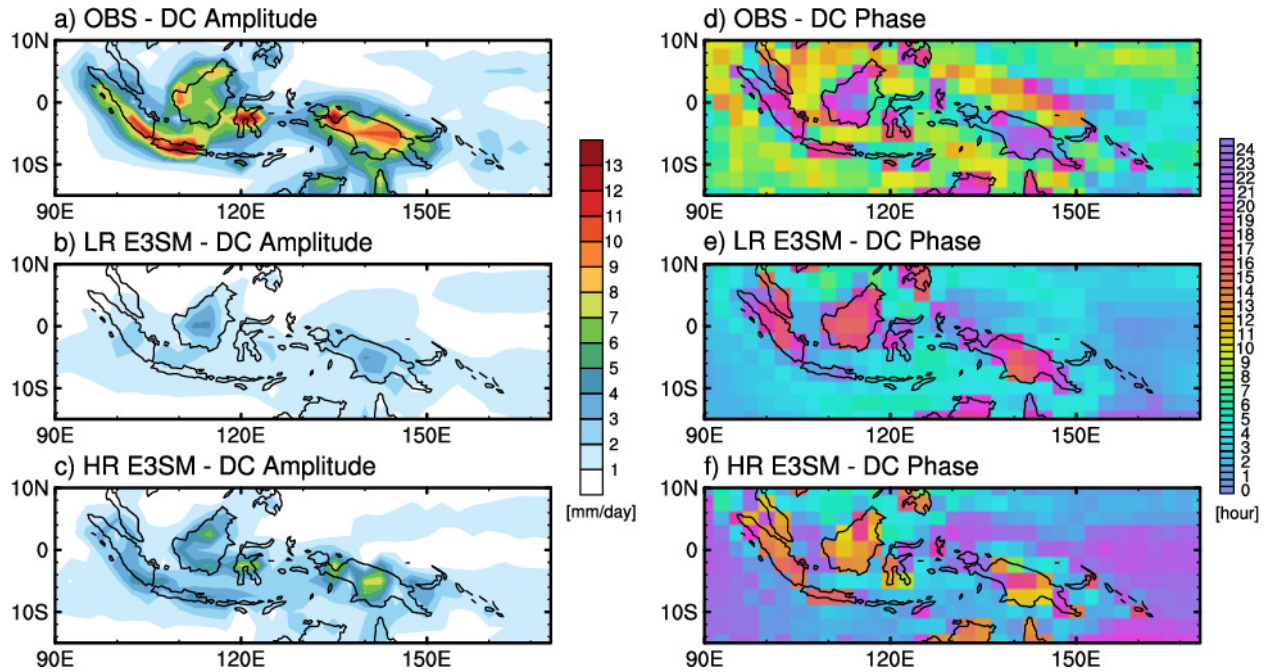
1040

1041 **Figure 5.** Contribution of each MSE budget term to the (a) propagation and (b) maintenance of  
 1042 the MJO during RMM phases 2 and 3 over the Indo-Pacific warm pool (20°S–10°N and 60–  
 1043 180°E) during NDJFMA. Blue and red bars indicate results from observations and E3SMv1,  
 1044 respectively.  
 1045



1046

1047 **Figure 6.** (top) Intraseasonal zonal wind (shaded,  $\text{m s}^{-1}$ ) and pressure velocity (contour,  $\text{Pa s}^{-1}$ )  
 1048 anomalies averaged over the equatorial band ( $10^{\circ}\text{S}$ - $10^{\circ}\text{N}$ ) composited for MJO phases 2 and 3:  
 1049 (left) ERA5 and (right) LR E3SMv1. (bottom) Same as the top panels, except for intraseasonal  
 1050 specific humidity anomalies ( $\text{g kg}^{-1}$ ) are shaded. The contour interval for pressure velocity is  
 1051  $0.005 \text{ Pa s}^{-1}$ . Line graphs at the bottom indicate column-integrated intraseasonal MSE ( $\times 10^4 \text{ kJ}$   
 1052  $\text{m}^{-2}$ ) and latent heat flux ( $\text{W m}^{-2}$ ) anomalies.



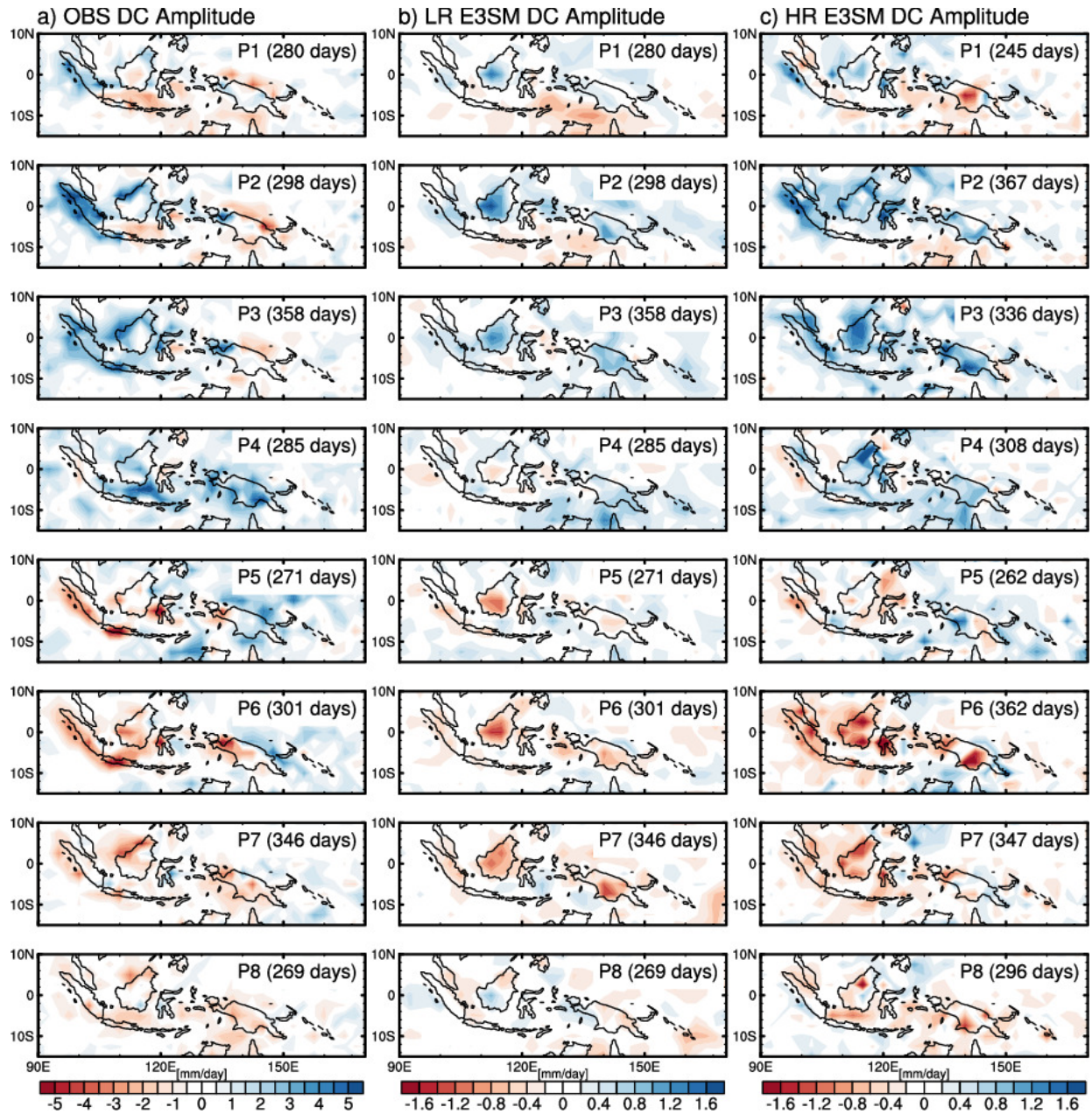
1053

1054

1055

1056

**Figure 7.** Climatological (left) amplitude ( $\text{mm day}^{-1}$ ) and (right) phase (hour) of the diurnal harmonic of precipitation from (top) TRMM, (middle) LR E3SMv1, and (bottom) HR E3SMv1 during NDJFMA.



1057

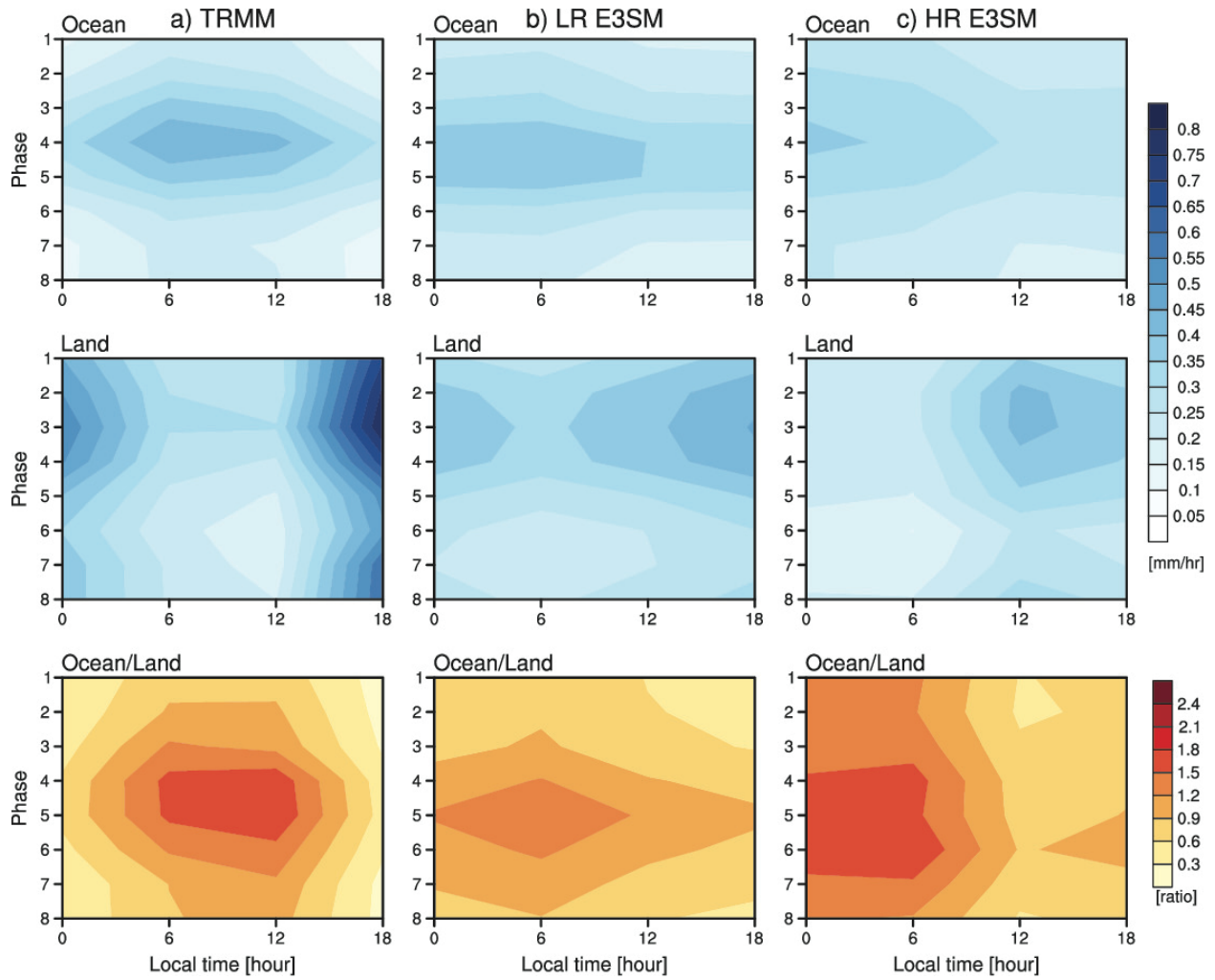
1058

1059

1060

1061

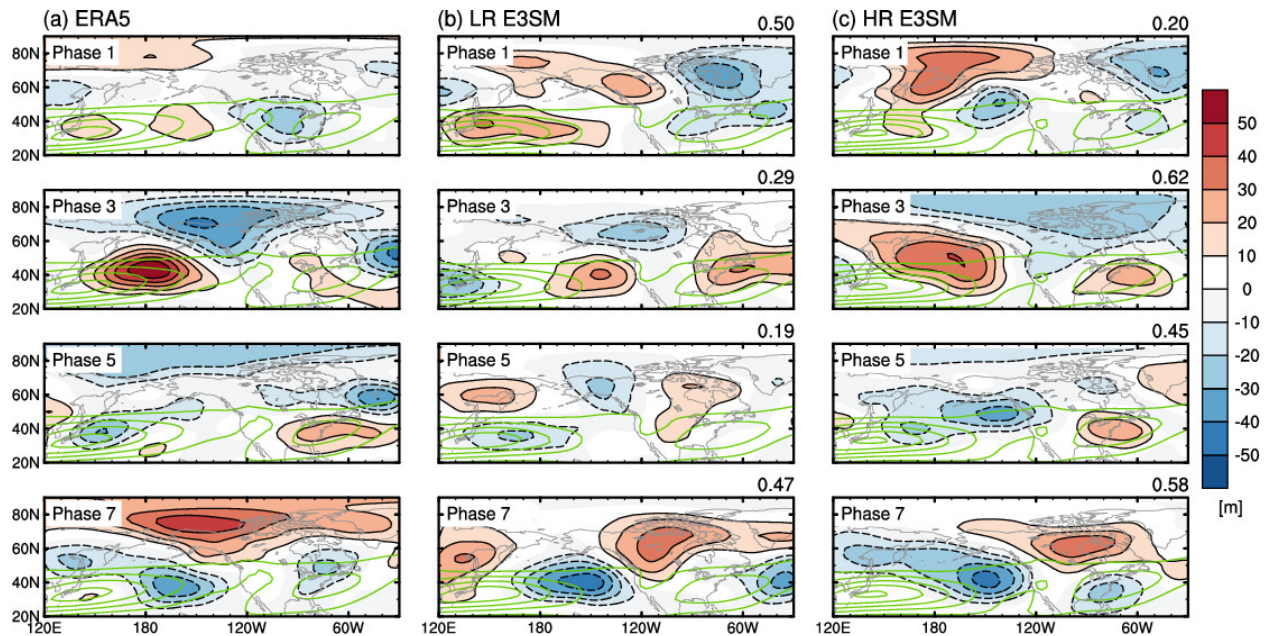
**Figure 8.** MJO life cycle composite maps of anomalous diurnal harmonic amplitude of precipitation ( $\text{mm day}^{-1}$ ) obtained from each RMM phase during NDJFMA: a) TRMM, b) LR E3SMv1, and c) HR E3SMv1.



1062

1063 **Figure 9.** Composite diurnal cycle of (upper) oceanic and (middle) land precipitation ( $\text{mm day}^{-1}$ )  
 1064 and (lower) their ratio over the western Maritime Continent ( $15^{\circ}\text{S}$ - $10^{\circ}\text{N}$ ,  $100$ - $120^{\circ}\text{E}$ ) as a  
 1065 function of MJO phase: a) TRMM and b) LR E3SMv1, and c) HR E3SMv1.

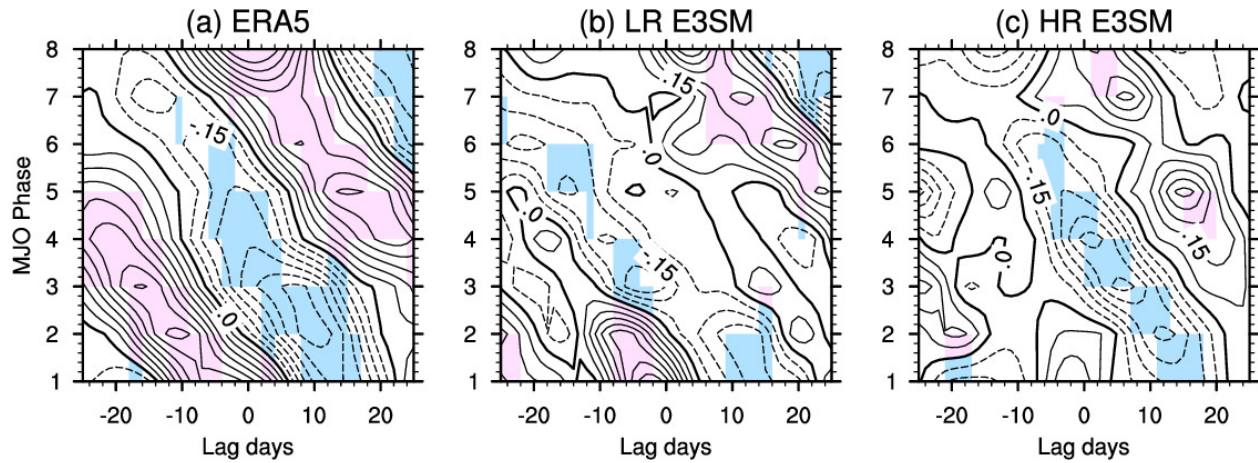
1066



1067

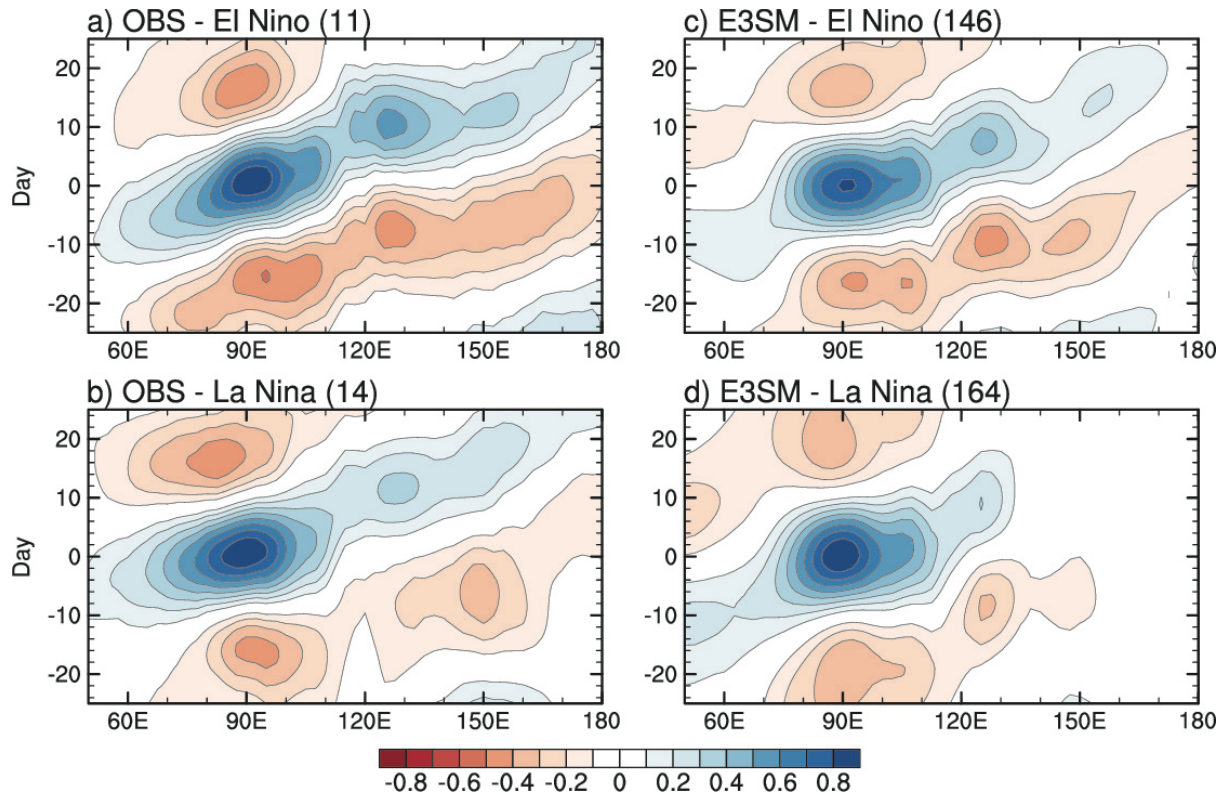
1068 **Figure 10.** MJO life cycle composite maps of 5-9 days average 500-hPa geopotential height  
 1069 anomalies (m, shaded) obtained from the selected four RMM phases during NDJFMA. Green  
 1070 contours indicate the climatological 300-hPa zonal wind ( $\text{m s}^{-1}$ , contour interval:  $10 \text{ m s}^{-1}$ ). Green  
 1071 contours begin from  $20 \text{ m s}^{-1}$ . a) ERA5, b) LR E3SMv1, and c) HR E3SMv1. For E3SM  
 1072 simulation results, the pattern correlation with the observed anomalies over the domain covered  
 1073 by the figures ( $20^{\circ}$ - $90^{\circ}$ N,  $120^{\circ}$ - $330^{\circ}$ E) is indicated at the right top of each panel.

1074



1075

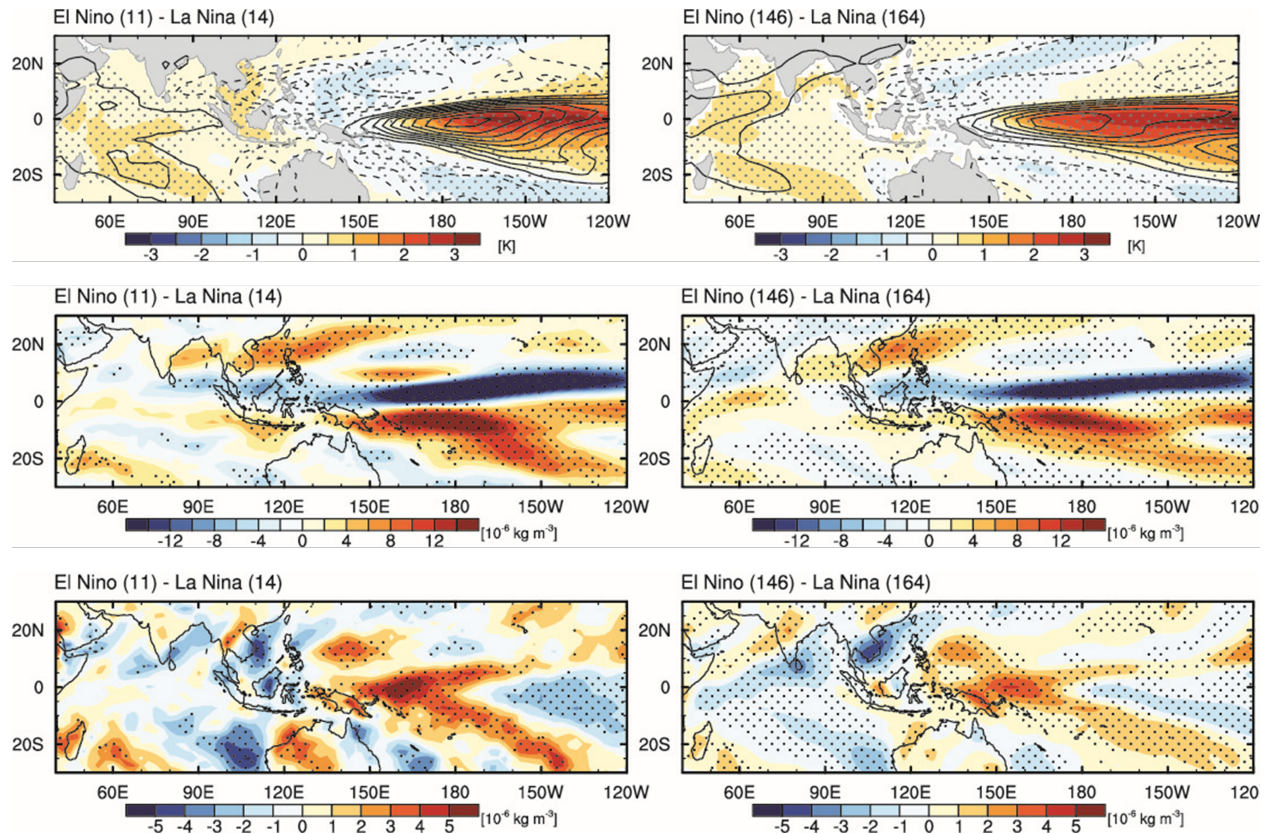
1076 **Figure 11.** Lead-lag composite of the PNA index around strong MJO days for each MJO phase  
1077 during NDJFMA: a) ERA5, b) LR E3SMv1, and c) HR E3SMv1. Pink and blue shading  
1078 indicates that positive and negative composite values are statistically significant at the 95%  
1079 confidence level.



1080

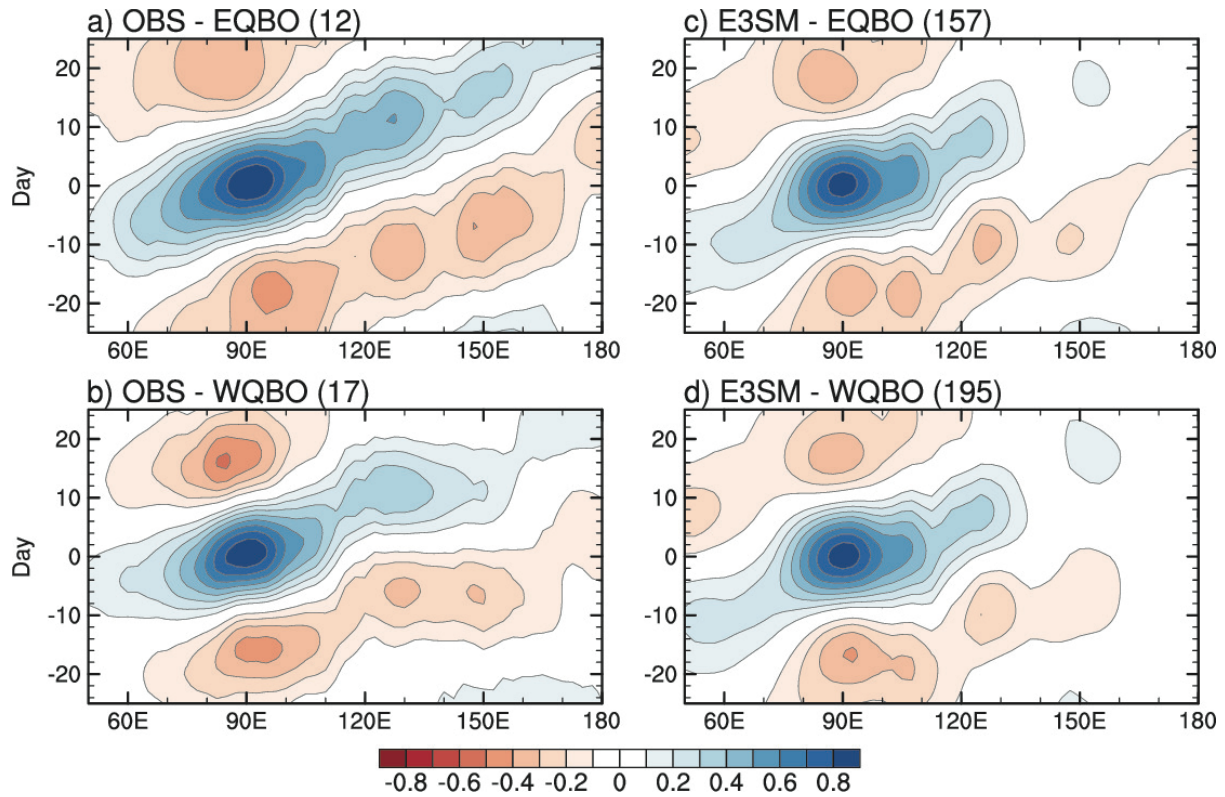
1081 **Figure 12.** Longitude–lag diagram of equatorial ( $10^{\circ}\text{S}$ – $10^{\circ}\text{N}$ ) OLR regressed against  
 1082 intraseasonal OLR anomalies in the Indian Ocean reference region ( $5^{\circ}\text{S}$ – $5^{\circ}\text{N}$ ,  $85$ – $95^{\circ}\text{E}$ ) during  
 1083 DJF for the El Niño and La Niña years from (left) observations and (right) 5-ensemble CMIP6  
 1084 Historical simulation made with LR E3SMv1. Numbers in parentheses denote the number El  
 1085 Niño and La Niña years. For observations and E3SMv1, El Niño and La Niña years are defined  
 1086 as the years with SST anomalies averaged over the Niño3.4 region ( $5^{\circ}\text{S}$ – $5^{\circ}\text{N}$ ,  $170$ – $120^{\circ}\text{W}$ ) being  
 1087 higher than its 0.5 standard deviation and lower than its -0.5 standard deviation, respectively.

1088



1089

1090 **Figure 13.** Differences between the El Niño and La Niña years in DJF mean state:(left)  
 1091 observations and (right) 5-ensemble CMIP6 Historical simulation made with LR E3SMv1. (top)  
 1092 SST (K, shaded) and precipitable water ( $\text{kg m}^{-2}$ , contour), (middle) meridional and (bottom)  
 1093 zonal gradient of precipitable water ( $\times 10^{-6} \text{ kg m}^{-3}$ ). Black dots indicate the differences are  
 1094 statistically significant at the 95% confidence level. Numbers in the parentheses denote the  
 1095 number of El Niño and La Niña years used in the analysis.



1096

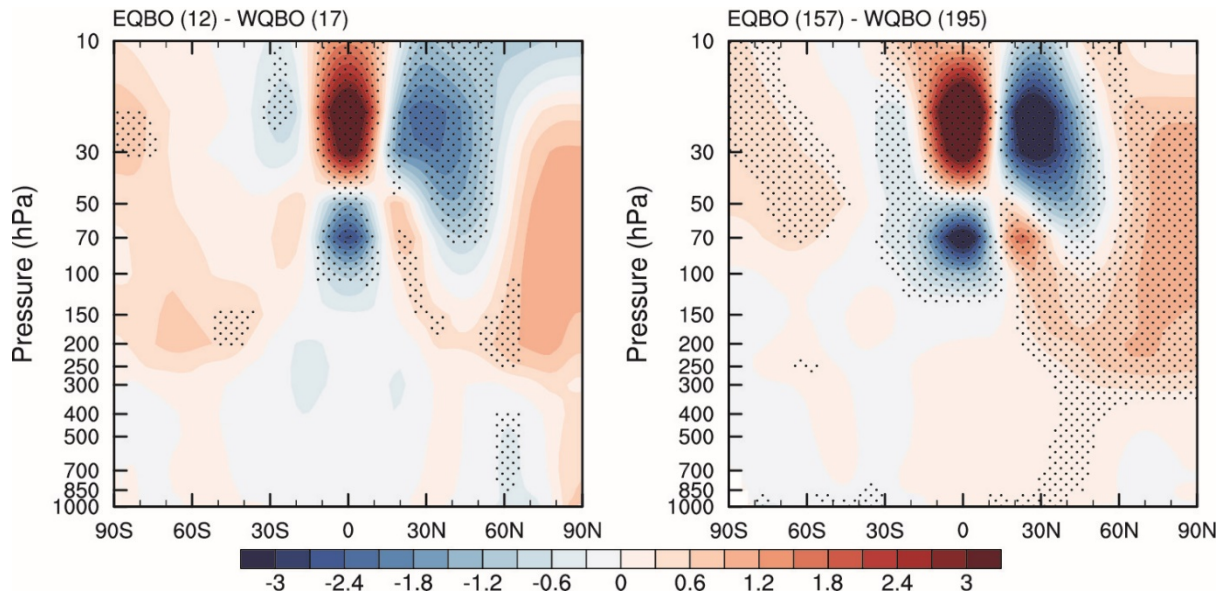
1097

1098

1099

**Figure 14.** Same as Figure 12, except for the (top) EQBO and (bottom) WQBO years obtained as the years with 50-hPa zonal wind anomalies averaged in the equatorial band ( $10^{\circ}\text{S}$ – $10^{\circ}\text{N}$ ) being higher than 0.5 standard deviation and lower than -0.5 standard deviation, respectively.

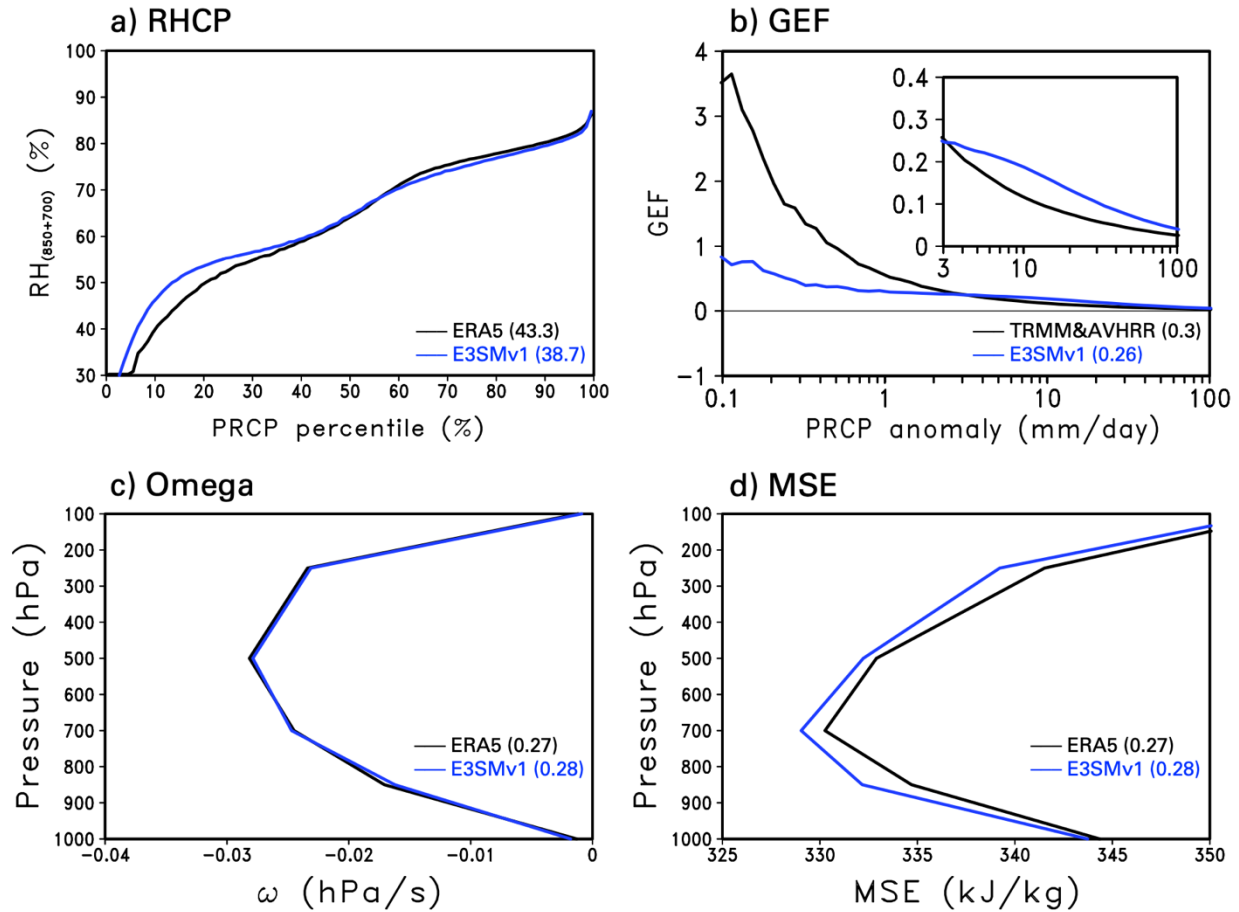
1100



1101

1102 **Figure 15.** Differences between the EQBO and WQBO years in DJF-mean zonal-mean  
1103 temperature (K): (left) observation and (right) 5-ensemble CMIP6 Historical simulation made  
1104 with LR E3SMv1. Black dots indicate shaded differences are statistically significant at the 95%  
1105 confidence level.

1106



1107

1108 **Figure 16.** Process-oriented MJO diagnostics: a) the relative humidity composite based on  
 1109 precipitation percentile (RHCP, %), b) the greenhouse enhancement factor (GEF, unitless), and  
 1110 the vertical profiles of the mean state c) pressure velocity ( $\text{hPa s}^{-1}$ ) and d) moist static energy  
 1111 (MSE,  $\text{kJ kg}^{-1}$ ) from observations (black) and LR E3SMv1 (blue). The pressure velocity and  
 1112 MSE profiles are used for the calculation of normalized gross moist stability (NGMS). The Indo-  
 1113 Pacific warm pool area ( $60^{\circ}\text{E}$ - $180^{\circ}\text{E}$ ,  $15^{\circ}\text{S}$ - $15^{\circ}\text{N}$ ) excluding land grid points is used for all the  
 1114 process-oriented diagnostics. Numbers in parentheses next to data labels denote the process-  
 1115 oriented metric values of RHCP, GEF, and NGMS.  
 1116